Starburst to Quiescent from HST/ALMA: Stars and Dust Unveil Minor Mergers in Submillimeter Galaxies at z ~ 4.5

Gómez-Guijarro, C.; Toft, S.; Karim, A.; Magnelli, B.; Magdis, G. E.; Jiménez-Andrade, E. F.; Capak, P. L.; Fraternali, F.; Fujimoto, S.; Riechers, D. A.; ...

Source / Izvornik: **Astrophysical Journal, 2018, 856**

Journal article, Published version
Rad u časopisu, Objavljena verzija rada (izdavačev PDF)

https://doi.org/10.3847/1538-4357/aab206

Permanent link / Trajna poveznica: https://urn.nsk.hr/urn:nbn:hr:217:090547

The Astrophysical Journal, 856:121 (18pp), 2018 April 1 https://doi.org/10.3847/1538-4357/aab206

Starburst to Quiescent from *HST*/ALMA: Stars and Dust Unveil Minor Mergers in Submillimeter Galaxies at $z \sim 4.5$

C. Gómez-Guijarro[1,2], S. Toft[1,2], A. Karim[3], B. Magnelli[3], G. E. Magdis[1,2,4], E. F. Jiménez-Andrade[2,5], P. L. Capak[6,7], F. Fraternali[8,9], S. Fujimoto[10], D. A. Riechers[11], E. Schinnerer[12], V. Smolčić[13], M. Aravena[14], F. Bertoldi[3], I. Cortzen[1,2], G. Hasinger[15], E. M. Hu[15], G. C. Jones[16,17], A. M. Koekemoer[18], N. Lee[1], H. J. McCracken[19,20], M. J. Michałowski[21], F. Navarrete[22], M. Pović[23,24], A. Puglisi[25], E. Romano-Díaz[3], K. Sheth[26], J. D. Silverman[27], J. Staguhn[28,29], C. L. Steinhardt[1,2], M. Stockmann[1,2], M. Tanaka[30], F. Valentino[1,2], E. van Kampen[25], and A. Zirm[1,31]

[1] Dark Cosmology Centre, Niels Bohr Institute, University of Copenhagen, Juliane Maries Vej 30, DK-2100 Copenhagen, Denmark; cgguijarro@dark-cosmology.dk
[2] Cosmic Dawn Center (DAWN), Niels Bohr Institute, University of Copenhagen, Copenhagen, Denmark
[3] Argelander-Institut für Astronomie, Universität Bonn, Auf dem Hügel 71, D-53121 Bonn, Germany
[4] Institute for Astronomy, Astrophysics, Space Applications and Remote Sensing, National Observatory of Athens, GR-15236 Athens, Greece
[5] International Max Planck Research School of Astronomy and Astrophysics at the Universities of Bonn and Cologne, Germany
[6] IPAC, 1200 E. California Blvd., Pasadena, CA 91125, USA
[7] California Institute of Technology, 1200 E. California Blvd., Pasadena, CA 91125, USA
[8] Department of Physics and Astronomy, University of Bologna, viale Bertu Pichat 6/2, I-40127 Bologna, Italy
[9] Kapteyn Astronomical Institute, University of Groningen, P.O. Box 800, 9700AV Groningen, The Netherlands
[10] Institute for Cosmic Ray Research, The University of Tokyo, Kashiwa, Chiba 277-8582, Japan
[11] Department of Astronomy, Cornell University, Space Science Building, Ithaca, NY 14853, USA
[12] Max Planck Institut für Astronomie, Königtuhl 17, D-69117, Heidelberg, Germany
[13] Department of Physics, Faculty of Science, University of Zagreb, Bijenička cesta 32, 10000 Zagreb, Croatia
[14] Núcleo de Astronomía, Facultad de Ingeniería y Ciencias, Universidad Diego Portales, Av. Ejército 441, Santiago, Chile
[15] Institute for Astronomy, University of Hawaii, 2680 Woodlawn Drive, Honolulu, HI 96822, USA
[16] Physics Department, New Mexico Institute of Mining and Technology, Socorro, NM 87801, USA
[17] National Radio Astronomy Observatory, 1003 Lopezville Road, Socorro, NM 87801, USA
[18] Space Telescope Science Institute, 3700 San Martin Drive, Baltimore, MD 21218, USA
[19] Sorbonne Universités, UPMC Univ Paris 06, UMR 7095, Institut d'Astrophysique de Paris F-75014 Paris, France
[20] CNRS, UMR 7095, Institut d'Astrophysique de Paris, F-75014 Paris, France
[21] Astronomical Observatory Institute, Faculty of Physics, Adam Mickiewicz University, ul. Słoneczna 36, 60-286 Poznań, Poland
[22] Max Planck Institut für Radioastronomie, Auf dem Hügel 69, D-53121 Bonn, Germany
[23] Ethiopian Space Science and Technology Institute (ESSTI), Entoto Observatory and Research Center (EORC), Astronomy and Astrophysics Research Division, P.O. Box 33679, Addis Ababa, Ethiopia
[24] Instituto de Astrofísica de Andalucía (IAA-CSIC), Glorieta de la Astronomía s/n, E-18008 Granada, Spain
[25] European Southern Observatory, Karl-Schwarzschild-Strasse 2, D-85748 Garching bei München, Germany
[26] NASA Headquarters, 300 E Street SW, Washington, DC 20546, USA
[27] Kavli Institute for the Physics and Mathematics of the Universe (WPI), The University of Tokyo Institutes for Advanced Study, The University of Tokyo, Kashiwa, Chiba 277-8583, Japan
[28] NASA Goddard Space Flight Center, Code 665, Greenbelt, MD 20771, USA
[29] Department of Physics and Astronomy, Johns Hopkins University, Baltimore, MD 21218, USA
[30] National Astronomical Observatory of Japan, 2-21-1 Osawa, Mitaka, Tokyo 181-8588, Japan
[31] Greenhouse Software, 3rd Floor, 110 5th Avenue, New York, NY 10011, USA
Received 2017 November 1; revised 2018 January 16; accepted 2018 February 20; published 2018 March 30

Abstract

Dust-enshrouded, starbursting, submillimeter galaxies (SMGs) at $z \geqslant 3$ have been proposed as progenitors of $z \geqslant 2$ compact quiescent galaxies (cQGs). To test this connection, we present a detailed spatially resolved study of the stars, dust, and stellar mass in a sample of six submillimeter-bright starburst galaxies at $z \sim 4.5$. The stellar UV emission probed by *HST* is extended and irregular and shows evidence of multiple components. Informed by *HST*, we deblend *Spitzer*/IRAC data at rest-frame optical, finding that the systems are undergoing minor mergers with a typical stellar mass ratio of 1:6.5. The FIR dust continuum emission traced by ALMA locates the bulk of star formation in extremely compact regions (median $r_e = 0.70 \pm 0.29$ kpc), and it is in all cases associated with the most massive component of the mergers (median $\log(M_*/M_\odot) = 10.49 \pm 0.32$). We compare spatially resolved UV slope (β) maps with the FIR dust continuum to study the infrared excess (IRX $= L_{IR}/L_{UV}$)–β relation. The SMGs display systematically higher IRX values than expected from the nominal trend, demonstrating that the FIR and UV emissions are spatially disconnected. Finally, we show that the SMGs fall on the mass–size plane at smaller stellar masses and sizes than the cQGs at $z = 2$. Taking into account the expected evolution in stellar mass and size between $z = 4.5$ and $z = 2$ due to the ongoing starburst and mergers with minor companions, this is in agreement with a direct evolutionary connection between the two populations.

Key words: galaxies: evolution – galaxies: formation – galaxies: high-redshift – galaxies: interactions – galaxies: ISM – galaxies: starburst

1. Introduction

Giant elliptical galaxies are the oldest, most massive galaxies in the local universe. Understanding their formation and evolution is one of the major challenges in contemporary galaxy evolution studies. They are uniformly old, red, and quiescent, i.e., void of star formation. Studies of their stellar

populations suggest that they formed in violent bursts of star formation at $z \sim 3$–5 (e.g., Thomas et al. 2005). Their evolution has been traced all the way back to $z \sim 4$ through the study of mass-complete samples of quiescent galaxies as a function of redshift (e.g., Brammer et al. 2011; van der Wel et al. 2014; Straatman et al. 2015; Davidzon et al. 2017).

Compared with their lower-redshift descendants, at $z \sim 2$, half of the most massive galaxies are already old, quiescent, and, furthermore, found to be extremely compact systems (e.g., Toft et al. 2007; van Dokkum et al. 2008; Szomoru et al. 2012). The brightest examples of these compact quiescent galaxies (cQGs) at $z \sim 2$ (for which follow-up spectroscopy has been possible) show clear post-starburst features, evidence of a starburst at $z > 3$ (e.g., Toft et al. 2012; van de Sande et al. 2013; Kriek et al. 2016; Belli et al. 2017; Toft et al. 2017; M. Stockmann et al. 2018, in preparation). Their subsequent evolution into local ellipticals is most likely dominated by passive aging of their stellar populations and merging with minor companions (e.g., Bezanson et al. 2009; Newman et al. 2012; Oser et al. 2012; Toft et al. 2012).

The most intense starbursts known are the so-called dusty star-forming galaxies (DSFGs), which are characterized by star formation rates (SFRs) of up to thousands of solar masses per year (see Casey et al. 2014a for a review). The best-studied DSFGs are the submillimeter galaxies (SMGs; e.g., Blain et al. 2002). Their high dust content absorbs the intense ultraviolet (UV) emission from the starburst and reradiates it at far-infrared/submillimeter (FIR/sub-mm) wavelengths (e.g., Swinbank et al. 2014), making the most intense starbursts easily detectable in sub-mm surveys to the highest redshift.

Following the discovery of a high-redshift tail in the SMG redshift distribution (e.g., Chapman et al. 2005; Capak et al. 2008, 2011; Daddi et al. 2009; Smolčić et al. 2012; Weiß et al 2013; Miettinen et al. 2015; Strandet et al. 2016; Brisbin et al. 2017), Toft et al. (2014) presented evidence for a direct evolutionary connection between $z \gtrsim 3$ SMGs and $z \sim 2$ cQGs based on the formation redshift distribution for the quiescent galaxies, number density arguments, and the similarity of the distributions of the two populations in the stellar mass–size plane (see also, e.g., Cimatti et al. 2008; Ricciardelli et al. 2010; Simpson et al. 2014, 2015; Ikarashi et al. 2015; Hodge et al. 2016; Oteo et al. 2016, 2017). However, as the latter was based on sizes derived from low-resolution data probing the rest-frame UV emission (which is likely biased toward unobscured, young stellar populations), confirmation using higher-quality data is crucial.

To test the proposed evolutionary connection, we here present deep, high-resolution *Hubble Space Telescope* (*HST*) and Atacama Large Millimeter/submillimeter Array (ALMA) follow-up observations of six of the highest-redshift SMGs from Toft et al. (2014), five of which are spectroscopically confirmed at $z \sim 4.5$. The data probe the distribution of the UV-bright stellar populations and the FIR dust continuum emission, which allows for a full characterization of the star formation and dust attenuation in the galaxies. The sources are drawn from the COSMOS field; thus, a wealth of deep ground- and space-based lower-resolution optical–mid-IR data are available, which we use to obtain stellar masses for the systems.

In two companion papers, we will explore the gas/dust distributions and kinematics of the sample (A. Karim et al. 2018, in preparation) and the detailed molecular gas properties of one of the sources (Jiménez-Andrade et al. 2018).

The layout of the paper is as follows. We introduce the sample, data, and methodology in Section 2. In Section 3, we present the rest-frame UV/FIR morphologies of the sample. The results based on the comparison of the dust as seen in absorption and emission are shown in Section 4. Stellar masses are discussed in Section 5. We show the evolutionary connection between SMGs and cQGs in Section 6. Additional discussion is presented in Section 7. We summarize the main findings and conclusions in Section 8.

Throughout this work, we adopted a concordance cosmology $[\Omega_\Lambda, \Omega_M, h] = [0.7, 0.3, 0.7]$ and Chabrier initial mass function (IMF; Chabrier 2003). The AB magnitude system was employed across the whole study (Oke 1974).

Table 1
Sample of Targeted SMGs in COSMOS

Source Name	Other Name	α(J2000)[a] (h:m:s)	δ(J2000)[a] (°:′:″)
AK03	⋯	10 00 18.74	+02 28 13.53
AzTEC1	AzTEC/C5	09 59 42.86	+02 29 38.2
AzTEC5	AzTEC/C42	10 00 19.75	+02 32 04.4
AzTEC/C159	⋯	09 59 30.42	+01 55 27.85
J1000+0234	AzTEC/C17	10 00 54.48	+02 34 35.73
Vd-17871	⋯	10 01 27.08	+02 08 55.60

Note.
[a] From Smolčić et al. (2017): AK03, AzTEC/C159, and Vd-17871 refer to the VLA 3 GHz peak position (Smolčić et al. 2015); AzTEC1 and AzTEC5 refer to the SMA 890 μm peak position (Younger et al. 2007); J1000+0234 refers to the PdBI ^{12}CO(4−3) emission-line peak position (Schinnerer et al. 2008).

2. Sample and Data

2.1. COSMOS SMG Sample

We selected a sample of six of the highest-redshift unlensed SMGs from Toft et al. (2014; see Table 1), which are part of the extensive (sub)millimeter interferometric and optical/millimeter spectroscopic follow-up campaigns in the COSMOS field (Scoville et al. 2007; Younger et al. 2007, 2008; Capak et al. 2008, 2011; Schinnerer et al. 2008; Riechers et al. 2010, 2014a; Smolčić et al. 2011, 2015; Yun et al. 2015). All of our sample sources had been spectroscopically confirmed to be at $4.3 \lesssim z \lesssim 4.8$, except AzTEC5 at a slightly lower (photometric) redshift (see Table 3). We refer the reader to Smolčić et al. (2015) for a detailed description of the selection of each source.

2.2. HST Data

HST WFC3/IR observations of AzTEC1, J1000+0234, and Vd-17871 were taken in the F125W and F160W bands at a two-orbit depth on each filter (program 13294; PI: A. Karim). For AK03 and AzTEC5, WFC3 F125W and F160W imaging were taken from the CANDELS survey (Grogin et al. 2011; Koekemoer et al. 2011). AzTEC/C159 was not in our *HST* program due to its faintness at near-IR wavelengths. Additionally, we included COSMOS *HST* ACS/WFC F814W images (Koekemoer et al. 2007) available for the full sample. At the redshift of the sources, these three bands probe the UV continuum regime in the range ∼140–300 nm (175–345 nm for AzTEC5).

In order to process the *HST* observations from our program, we made use of the DrizzlePac 2.0 package (Gonzaga et al. 2012). First, we assured a good alignment between the four dithered frames on each band using the `TweakReg` task. Next, we combined the frames with `AstroDrizzle`,

employing the same parameters as used in the CANDELS reduction procedure: final_scale = 0.06 and final_pixfrac = 0.8 (Koekemoer et al. 2011).

For the purpose of this work, it is important that all three bands are properly aligned, sharing a common World Coordinate System (WCS) frame with accurate absolute astrometry. In order to guarantee the absolute astrometric accuracy, we chose the COSMOS ACS F814W image as the reference frame. The fundamental astrometric frame for COSMOS uses the CFHT Megacam *i*-band image (Capak et al. 2007). The latter is tied to the USNO-B1.0 system (Monet et al. 2003), which is also tied to the VLA 1.4 GHz image (Schinnerer et al. 2004), ensuring an absolute astrometric accuracy of 0.″05–0.″1 or better, corresponding to ∼1–1.5 pixel for our pixel scale. To align the F125W and F160W images to the F814W WCS, we used TweakReg along with SExtractor (Bertin & Arnouts 1996) catalogs of the three bands, with the F814W catalog and frame as references. Once the three bands shared the same WCS frame, we propagated the WCS solution back to the original flt.fits frames using the TweakBack task and then ran AstroDrizzle once again to produce the final drizzled images. In the case of AK03 and AzTEC5, where the F125W and F160W data came from CANDELS, this alignment procedure is not necessary, since the images are already matched to the COSMOS WCS. The final drizzled images in the three bands were resampled to a common grid and a pixel scale of 0.″06 pixel^{-1} using SWarp (Bertin 2010).

2.3. ALMA Data

Our galaxies were observed in ALMA's Cycle 2 as part of Cycle 1 (program 2012.1.00978.S; PI: A. Karim). We used the ALMA band 7 and tuned the correlator such that a single spectral window (SpW) would cover the [C II] line emission of our galaxies, while three adjacent SpWs with a total bandwidth of 5.7 GHz would be used for continuum detection. These continuum SpWs are those analyzed in our study, while the [C II] line data cubes are presented in A. Karim et al. (2018, in preparation).

All observations were taken in 2014 June using 34 12 m antennas in configuration C34-4 with a maximum baseline of ∼650 m. For all galaxies, J1058+0133 and J1008+0621 were used as bandpass and phase calibrators, respectively. In contrast, the flux calibrator is not the same for all galaxies, varying among Titan, J1058+0133, Ceres, and Pallas. Calibration was performed with the Common Astronomy Software Applications (CASA; version 4.2.2) using the scripts provided by the ALMA project. Calibrated visibilities were systematically inspected, and additional flaggings were added to the original calibration scripts. Flux calibrations were validated by checking the flux density accuracies of our phase and bandpass calibrators. Continuum images were created by combining the three adjacent continuum SpWs with the CASA task CLEAN in multifrequency synthesis imaging mode and using a standard Briggs weighting scheme with a robust parameter of −1.0. The effective observing frequencies, synthesized beams, and resulting noise of these continuum images are listed in Table 2.

Each galaxy yields a significant continuum detection signal-to-noise ratio (S/N) > 10 at the phase center of our images. Their fluxes were measured via 2D Gaussian fits using the python package PyBDSF and are given in Table 2. These fluxes are consistent with the measured 850 μm fluxes from the S2COSMOS/SCUBA2 survey (J. M. Simpson et al. 2018, in preparation). This suggests that there is no extended emission that is resolved out in the higher-resolution ALMA observations.

In terms of the WCS, we do not expect a significant offset in the ALMA absolute astrometry with respect to the COSMOS WCS. The main source of uncertainty for the relative astrometry between ALMA and *HST* is the uncertainty in the *HST* absolute astrometry with respect to the COSMOS WCS, which is <0.″1, as shown in the previous section. Schreiber et al. (2017) tested the relative astrometry between an ALMA single pointing and an *HST* image tied to the COSMOS WCS. Following Schreiber et al. (2017), at our S/N and resolution, the combined pointing accuracy between our ALMA and *HST* images is <0.″12, corresponding to <2 pixels for our pixel scale.

2.4. PSF Matching

The *HST* data span three different bands from two different instruments; consequently, the spatial resolution is different. It is essential to compare the same physical regions when obtaining resolved color information. We therefore degraded the ACS F814W and WFC3 F125W images to the resolution of the WFC3 F160W data (0.″18 FWHM), which has the broadest point-spread function (PSF). First, we created a stacked PSF in the different bands, selecting stars that were not saturated and did not show irregularities on their light profiles. Second, we derived the kernels to match the ACS F814W and WFC3 F125W PSFs to the PSF in the WFC3 F160W image using the task PSFMATCH in IRAF. We applied a cosine bell function tapered in frequency space to avoid introducing artifacts in the resulting kernel from the highest frequencies. To get the best size for the convolution box, we iterated over different values. Finally, we implemented the kernel on the ACS F814W and WFC3 F125W images. The matched PSF FWHMs in the different bands deviate by less than 2%.

ALMA continuum images also show different spatial resolution compared to that in the PSF-matched *HST* images (median synthesized beam size of 0.″30 × 0.″27 versus 0.″18 FWHM, respectively). It is important to perform the measurements in the same physical regions when comparing *HST* and ALMA photometry as well, such as to derive rest-frame FIR/UV ratios. When this is required, we used *HST* images matched to the resolution of the ALMA continuum images constructed following the procedure explained above. In this case, the kernel was computed from the WFC3 F160W PSF and the ALMA clean beam and then applied to the PSF-matched *HST* images. The matched PSF FWHMs in the *HST* and ALMA images deviate by less than 2%.

2.5. Adaptive Smoothing

We applied a smoothing technique to the *HST* images to enhance the S/N and improve our ability to detect low surface brightness features and color gradients between neighboring pixels.

The code employed for this purpose was ADAPTSMOOTH (Zibetti 2009), which smooths the images in an adaptive fashion, meaning that at any pixel, only the minimum smoothing length to reach the S/N requested is applied. In this way, the images retain the original resolution in regions

Table 2
ALMA Continuum Image Properties

Source Name	ν_{obs} (Ghz)	Beam Size (arcsec × arcsec)	σ (mJy beam^{-1})	S_{870}^{ALMA}[a] (mJy)	S_{850}^{SCUBA2}[b] (mJy)
AK03	337.00	0.29 × 0.27	0.17	2.3(2.7) ± 0.2	2.4(1.7) ± 0.6
AzTEC1	344.67	0.25 × 0.22	0.47	14.5(15.7) ± 0.2	14.8(14.3) ± 1.2
AzTEC5	301.78	0.47 × 0.28	0.089	7.2(12.4) ± 0.2	13.2(13.1) ± 0.7
AzTEC/C159	349.67	0.28 × 0.27	0.20	6.9(7.1) ± 0.2	6.8(5.5) ± 1.3
J1000+0234	349.85	0.30 × 0.23	0.11	7.6(7.8) ± 0.2	6.7(5.8) ± 1.0
Vd-17871	345.75	0.35 × 0.31	0.21	5.2(5.6) ± 0.2	4.8(3.9) ± 0.9

Notes.
[a] In parentheses, conversion into 850 μm fluxes, assuming a standard Rayleigh–Jeans slope of 3.5.
[b] In parentheses, deboosted fluxes.

where the S/N is high, and only low-S/N regions are smoothed.

We required a minimum S/N = 5 and a maximum smoothing length of two neighboring pixels in the code. The former holds true for uncorrelated noise, which is not the case for the drizzled *HST* images analyzed here. In our images, the chosen value of 5 corresponds to S/N ∼ 2 when taking into account the noise correlation and pixelation effects in the code. The chosen smoothing length prevents cross-talking between pixels, also reduced by calculating the median of the pixel distribution inside the smoothing radius as opposed to the mean. Such a smoothing length was chosen to match the resolution in the *HST* data, so the smoothing technique does not smear out the images.

We generated a smoothing mask for each band, which is a mask of the required smoothing length to reach the requested minimum S/N for each pixel. When applying a mask to the images, the pixels that do not reach the minimum S/N level are blanked out by the code. If a pixel reached the minimum S/N in at least two bands, we replaced the smoothing length in the mask by the maximum value of them. This guarantees that the same physical regions are probed in different bands, at the same time maintaining the signal if a pixel is above the minimum S/N in only one band.

2.6. Additional Photometric Data

A series of additional multiwavelength-imaging data sets in the optical/IR were employed in this work: the Subaru Hyper-Suprime-Cam (HSC) from the HSC Subaru Strategic Program (SSP) team and the University of Hawaii (UH) joint data set in the *g*, *r*, *i*, *z*, and *y* bands (Tanaka et al. 2017), with spatial resolutions (seeing FWHM) of 0.″92, 0.″57, 0.″63, 0.″64, and 0.″81, respectively; the UltraVISTA DR3 survey (McCracken et al. 2012) covering the near-IR *J*, *H*, and K_s bands, which have resolutions of 0.″8, 0.″7, and 0.″7, respectively; and the *Spitzer* Large Area Survey with Hyper-Suprime-Cam (SPLASH; P. L. Capak et al. 2018, in preparation) mid-IR *Spitzer*/IRAC 3.6 and 4.5 μm, with PSF FWHMs of 1.″66 and 1.″72, respectively.

3. Morphology

The high spatial resolution of the *HST* and ALMA data (0.″18 FWHM versus a median synthesized beam size of 0.″30 × 0.″27, respectively) allows for detailed studies of the distributions of both obscured and unobscured star formation in the galaxies. The *HST* F814W, F125W, and F160W images sample the rest-frame stellar UV, which traces unextincted to moderately extincted star formation, and ALMA band 7 (∼870 μm) samples the rest-frame FIR dust continuum (at ∼160 μm for $z = 4.5$), which traces highly obscured star formation. In Figure 1, we compare these two complementary probes for the objects observed in our *HST* program (all except AzTEC/C159). The *HST* images were PSF-matched and smoothed as described in Sections 2.4 and 2.5.

Qualitatively, the comparison of *HST* and ALMA images suggests important differences in the morphologies. The rest-frame UV stellar emission appears extended and irregular, whereas the rest-frame FIR dust continuum appears very compact. Recently, Hodge et al. (2016) found similar results by comparing stellar morphologies from *HST* F160W and ALMA 870 μm images in a sample of 16 SMGs at a median redshift of $z \sim 2.5$. Chen et al. (2015) presented similar results regarding the stellar component at rest-frame optical in a larger sample of 48 SMGs at $z = 1$–3.

AK03, AzTEC5, J1000+0234, and Vd-17871 show evidence of two major neighboring components in the rest-frame UV. According to the available spectroscopic redshifts, or photometric redshifts compatible within the uncertainties when we lack spectroscopic confirmation, these components are consistent with being at the same redshift (see Table 3). They also show irregularities and features connecting them (see Figure 1). Therefore, it seems very plausible that they are interacting and merging. In addition, AzTEC1 displays a secondary fainter companion toward the north detected in all three *HST* bands and *Spitzer*/IRAC. Furthermore, AK03, AzTEC5, and J1000+0234 show additional low-S/N companions detected in all of the *HST* bands (marked with arrows in Figure 1).

All together, the full sample is consistent with being multiple-component interacting systems. In Section 5, we discuss the stellar mass estimates for the different components of each source. Being able to distinguish the components in the lower-resolution data sets, especially in the case of the IRAC bands that trace the rest-frame optical, we obtain stellar masses that are large enough to support the merger scenario, as opposed to patches of a single disk or other form of highly extincted single structure (Marques-Chaves et al. 2018).

The compact rest-frame FIR emission, tracing the bulk of the star formation in the system, is always associated with the reddest UV component but often spatially offset and not coinciding with the reddest part of the galaxy. This lack of spatial coincidence between the UV and FIR emission is explored further in Section 4.

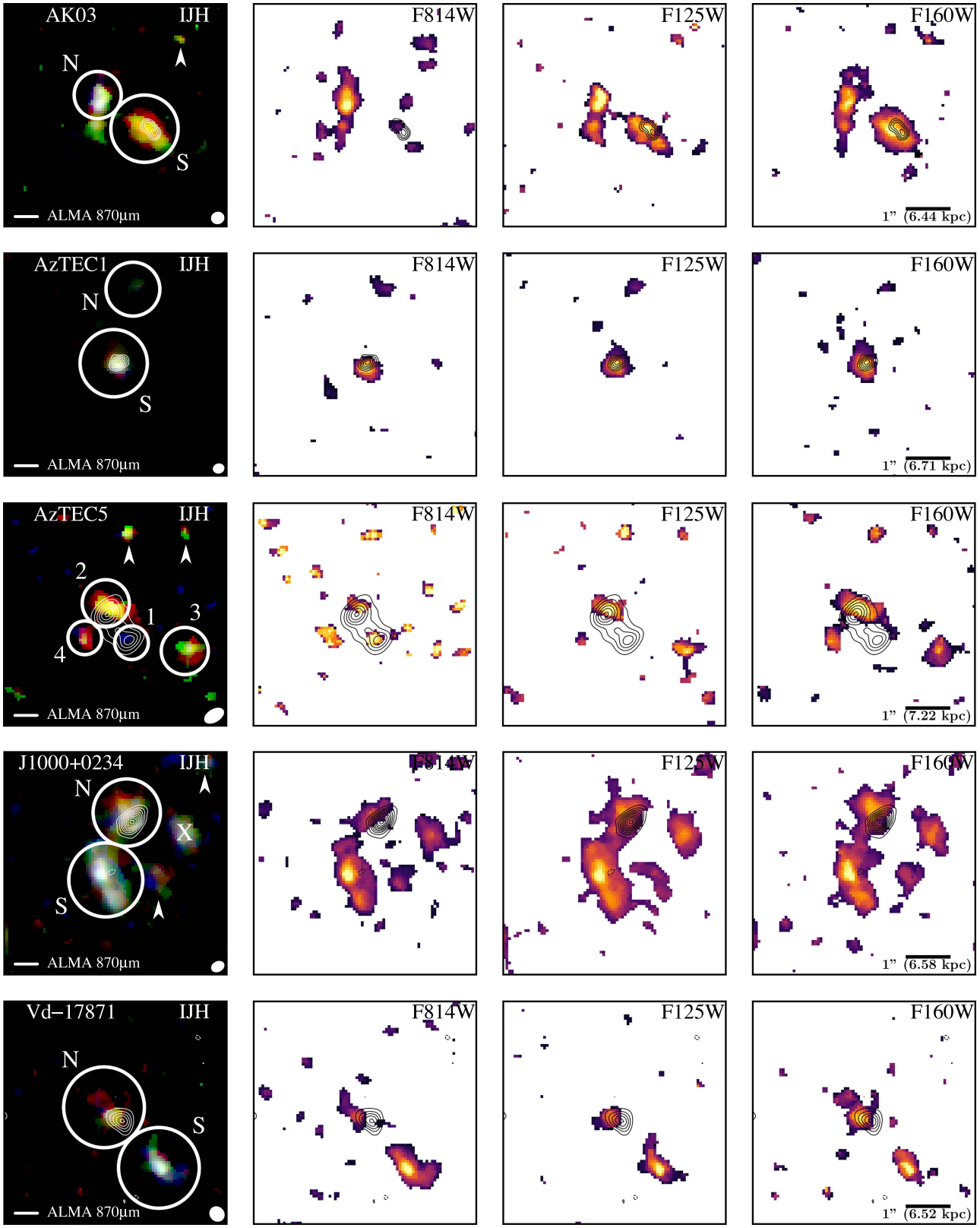

Figure 1. F814W, F125W, and F160W images of the five sources observed with *HST* and the RGB color composite assembled from these three bands. ALMA band 7 ($\sim$870 μm) contours are overlaid. The images are scaled from S/N = 2 to 75% of the peak value. The contours shown start at $\pm 3\sigma$ and go in steps of 1σ (AK03 and AzTEC1) or 3σ (AzTEC5, J1000+0234, and Vd-17871). Different components considered for each source are circled and labeled in the RGB image, and potential additional companions are marked with an arrow. The J1000+0234 component confirmed at a lower redshift is labeled with an X. The ALMA beam size is shown in the bottom left corner. North is up, east is to the left, and the images have a size of $5'' \times 5''$.

Table 3
Properties of the Stellar Components

Source Name	z_{spec}[a]	z_{phot}[b]	β	SFR_{UV} ($M_\odot$ yr^{-1})	L_{IR}[c] (10^{12} $L_\odot$)	SFR_{IR}[c] ($M_\odot$ yr^{-1})	M_{dust}[c] (10^8 $M_\odot$)	$\log(M_*/M_\odot)$[d]	$M_*/M_{*,prim}$[e]
*AK03-S	⋯	4.40 ± 0.10	$0.98^{+0.49}_{-0.39}$	25.5 ± 6.5	$1.2^{+8.1}_{-0.6}$	120^{+810}_{-60}	50^{+29}_{-35}	$10.76^{+0.08}_{-0.08}$	⋯
AK03-N	4.747	$4.75^{+0.08}_{-0.07}$	$-1.73^{+0.16}_{-0.16}$	53.4 ± 4.1	⋯	⋯	⋯	$9.55^{+0.06}_{-0.06}$	1:16.2
*AzTEC1-S	4.3415	⋯	$-1.16^{+0.18}_{-0.17}$	45.0 ± 4.0	$24.0^{+8.3}_{-6.2}$	2400^{+830}_{-620}	50^{+13}_{-10}	$10.58^{+0.10}_{-0.10}$	⋯
AzTEC1-N	⋯	$3.77^{+0.32}_{-0.22}$	$-2.6^{+1.0}_{-1.1}$	8.5 ± 3.3	⋯	⋯	⋯	$9.56^{+0.16}_{-0.20}$	1:10.5
*AzTEC5-1	⋯	⋯	< -3.2[f]	>4.2[f]	$7.9^{+1.6}_{-2.0}$[g]	790^{+160}_{-200}[g]	$9.5^{+2.0}_{-2.5}$[g]	$10.40^{+0.16}_{-0.12}$	⋯
*AzTEC5-2	⋯	$3.63^{+0.14}_{-0.15}$	$1.6^{+1.3}_{-1.2}$	2.1 ± 3.7	$13.2^{+2.7}_{-3.4}$[g]	1320^{+270}_{-340}[g]	$15.8^{+3.3}_{-4.1}$[g]	$9.92^{+0.10}_{-0.10}$	1:3.0
AzTEC5-3	⋯	$4.02^{+0.08}_{-0.08}$	$-0.25^{+1.1}_{-0.78}$	3.8 ± 2.6	⋯	⋯	⋯	$9.78^{+0.08}_{-0.10}$	1:4.2
AzTEC5-4	⋯	$3.66^{+0.40}_{-0.43}$	$-1.12^{+0.66}_{-0.52}$	5.2 ± 2.1	⋯	⋯	⋯	$9.59^{+0.08}_{-0.06}$	1:6.5
*AzTEC/C159	4.567	⋯	> -1.2[h]	<33[h]	$7.4^{+2.1}_{-1.7}$	740^{+210}_{-170}	$25.0^{+6.0}_{-5.0}$	$10.65^{+0.08}_{-0.08}$	⋯
*J1000+0234-N	4.539	⋯	$-1.01^{+0.39}_{-0.32}$	52.6 ± 8.5	$4.4^{+12}_{-3.2}$	440^{+1200}_{-320}	50^{+110}_{-34}	$10.14^{+0.08}_{-0.08}$	⋯
J1000+0234-S	4.547	$4.48^{+0.03}_{-0.03}$	$-2.04^{+0.12}_{-0.11}$	147.6 ± 7.4	⋯	⋯	⋯	$9.16^{+0.06}_{-0.08}$	1:9.5
*Vd-17871-N	4.621	$4.49^{+0.04}_{-0.03}$	$-0.59^{+0.35}_{-0.31}$	22.1 ± 4.0	$11.2^{+2.9}_{-2.3}$	1120^{+290}_{-230}	$12.6^{+3.2}_{-2.6}$	$10.04^{+0.10}_{-0.10}$	⋯
Vd-17871-S	4.631	$4.41^{+0.08}_{-0.09}$	$-2.27^{+0.22}_{-0.23}$	59.3 ± 5.5	⋯	⋯	⋯	$9.49^{+0.18}_{-0.30}$	1:3.5

Notes. Component names preceded by $*$ refer to those with an ALMA counterpart.
[a] Spectroscopic redshift references: AK03-N from Lyα by Smolčić et al. (2015); AzTEC1-S from [C II], also ^{12}CO(4–3) and ^{12}CO(5–4), by Yun et al. (2015); AzTEC/C159 from [C II] by A. Karim et al. (2018, in preparation), see also ^{12}CO(2–1) and ^{12}CO(5–4) by Jiménez-Andrade et al. (2018) and Lyα by Smolčić et al. (2015); J1000+0234-N from [C II] by A. Karim et al. (2018, in preparation), see also ^{12}CO(4–3) by Schinnerer et al. (2008) and Lyα by Capak et al. (2008); J1000+0234-S from Lyα by Capak et al. (2008); Vd-17871-N from [C II] by A. Karim et al. (2018, in preparation), see also Smolčić et al. (2015); Vd-17871-S from Lyα by A. Karim et al. (2018, in preparation), see also Smolčić et al. (2015).
[b] Photometric redshift references: AK03-S from Smolčić et al. (2015), who found $z_{phot} = 4.40 \pm 0.10$ or 4.65 ± 0.10, depending on the template used; AzTEC1-N calculated in this work, where the uncertainties correspond to the 1σ percentiles of the maximum-likelihood distribution and the redshift distribution spans the range $3.2 < z < 4.7$; AK03-N, AzTEC5-2, AzTEC5-3, and AzTEC5-4 from the 3D-*HST* survey catalog (Brammer et al. 2012; Skelton et al. 2014; Momcheva et al. 2016); J1000+0234-S, Vd-17871-N, and Vd-17871-S from the COSMOS2015 catalog (Laigle et al. 2016). AzTEC/C159, J1000+0234-N, and AzTEC5-1 have no counterpart in the COSMOS2015 catalog. For both 3D-*HST* and COSMOS2015 estimates, the listed uncertainties correspond to the 1σ percentiles.
[c] From Smolčić et al. (2015) (Toft et al. 2014 for AzTEC5) FIR SEDs covering 100 μm–1.1 mm, updated with new 850 μm fluxes from the S2COSMOS/SCUBA2 survey (J. M. Simpson et al. 2018, in preparation); L_{IR} (integrated from rest frame 8–1000 μm) and M_{dust} are inferred using the Draine & Li (2007) dust model, then SFR_{IR} is calculated using the L_{IR}-to-SFR_{IR} conversion from Kennicutt (1998) for a Chabrier IMF.
[d] Stellar mass uncertainties do not reflect systematics due to the SED fitting assumptions (i.e., stellar population synthesis models, IMF, or SFH).
[e] Stellar mass ratio between the quoted and most massive components ($M_{*,prim}$).
[f] Limits from detection in F814W and upper limits in F125W and F160W.
[g] AzTEC5-1 accounts for 30% and AzTEC5-2 for 50% of the total values for this source following our GALFIT ALMA continuum image modeling (see Section 4.2).
[h] Limits from UltraVISTA DR3 photometry.

There are no additional sub-mm detections within the ALMA primary beam at the current sensitivity; thus, we discard equally bright (close to the phase center) or brighter (away from the phase center) companion DSFGs at distances larger than those showed in the $5'' \times 5''$ images in Figure 1.

3.1. UV Stellar Components

In this section, we provide a detailed discussion of the individual systems and their subcomponents detected in the *HST* data (see Figure 1 and Table 3).

AK03: This system has two main UV components separated by $\sim 1''$ (AK03-N and AK03-S), with the F125W image suggesting a bridge connecting the two at an integrated $S/N = 2.4$. The spectroscopic confirmation refers to AK03-N, but AK03-S has a comparable photometric redshift (Smolčić et al. 2015; see Section 5.3). All of these may be considered evidence for a merger. The dust continuum emission is associated with AK03-S and shows two very compact emission peaks (unresolved at the current resolution), whereas AK03-N remains undetected. Therefore, the bulk of the star formation is associated with AK03-S.

AzTEC1: The source shows a compact UV component (AzTEC1-S) and a very faint companion source $\sim 2''$ toward the north, which is detected at $2 < S/N < 3$ in all three *HST* bands (AzTEC1-N). Despite the low S/N of this companion feature being detected in all three bands, the probability of being spurious is $\sim 10^{-5}$. More importantly, it is detected at $S/N > 3$ in the HSC r, i, and z bands and *Spitzer*/IRAC data, confirming that it is a real source. We derived a photometric redshift consistent with lying at the same redshift as AzTEC1-S (Yun et al. 2015) within the uncertainties (see Section 5.3). The rest-frame FIR emission is also compact and centered on AzTEC1-S.

AzTEC5: For this system, three main UV components are detected in all three *HST* bands (AzTEC5-2, AzTEC5-3, and AzTEC5-4), and a fourth component is detected only in F814W (AzTEC5-1). AzTEC5 is the only source in our sample that lacks spectroscopic confirmation, but photometric redshift estimation indicates a plausible solution for all four components at the same redshift (see Section 5.3). The irregular rest-frame UV morphology of AzTEC5-2 and AzTEC5-4, with emission connecting both in F160W, is suggestive of an ongoing merger. The rest-frame FIR has three emission peaks: two bright peaks associated with AzTEC5-1 and AzTEC5-2 and a fainter peak between them, which is not detected in any *HST* bands. Besides, the FIR peaks related to AzTEC5-1 and AzTEC5-2 are aligned with the position of the two peaks in the IRAC images, suggesting that the bulk of the stellar mass is associated with these two components, which are probably merging.

AzTEC/C159: As mentioned in Section 2.2, this source was excluded from the *HST* program and remains undetected in the

F814W band image, so we do not have any constraints on its UV morphology. The rest-frame FIR emission is compact and associated with detections in the IRAC bands.

J1000+0234: This system has three main UV components. J1000+0234-N and J1000+0234-S are spectroscopically confirmed at the same redshift (Capak et al. 2008; Schinnerer et al. 2008; A. Karim et al. 2018, in preparation), and J1000+0234-X is a foreground source at $z_{\rm spec} = 1.41$ (Capak et al. 2008). An additional companion is detected west of J1000+0234-S in all three *HST* bands, but the HSC images show diffuse features rather than a concentrated source, consistent with Capak et al. (2008). The north and south components show a connection between them in all three *HST* bands, suggesting a merger. The rest-frame FIR emission is compact and associated with J1000+0234-N.

Vd-17871: This system has two main UV components $\sim$1.″5 apart (Vd-17871-N and Vd-17871-S), both with elongated morphologies. Both the north and the south components are spectroscopically confirmed at the same redshift (Smolčić et al. 2015; A. Karim et al. 2018, in preparation). The compact rest-frame FIR emission is associated with the north component.

3.2. SED Fitting

Having disentangled different stellar components at rest-frame UV wavelengths, we performed photometry in the lower-resolution data sets mentioned in Section 2.6, aiming at fitting the resulting spectral energy distributions (SEDs) to constrain stellar masses for every major stellar component (see Table 3), corresponding to those circled in Figure 1. In the case of *Spitzer*/IRAC, with a significantly lower resolution, the components appear blended, so it is particularly important to know the number of them to properly deblend the fluxes.

From the g to the $K_{\rm s}$ bands, the sources are resolved into the stellar components defined from the rest-frame UV *HST* data, appearing unresolved themselves but separated enough so potential blending is not a concern. To estimate the fluxes in these bands, we carried out aperture photometry. The size of the apertures varied for each component and source, being the same across bands, and correspond to those plotted in Figure 1. We chose the apertures in the $K_{\rm s}$ band to be as large as possible, enclosing the component we wanted to study without overlapping with a neighboring component aperture. We performed aperture corrections for every band. In order to do so, we traced the growth curve of a PSF in the different bands and applied a correction factor to the fluxes accounting for the missing flux outside the aperture. We performed aperture corrections on each band instead of measuring in PSF-matched data to take advantage of the resolution, important for this kind of multiple-component system, that otherwise would be degraded to the lowest-resolution band. The uncertainties in the magnitudes were derived from empty aperture measurements. To assure a good SED fit, we only use detections above 3σ (upper limits are included in Figure 2).

For the blended *Spitzer*/IRAC 3.6 and 4.5 μm images, we employed the magnitudes from a PSF model using the two-dimensional surface brightness distribution fitting algorithm `GALFIT` (Peng et al. 2002). We required at least a 5σ detection to perform the fit, which was the case for all sources in the 3.6 and 4.5 μm bands. The number of PSFs was set to the number of stellar components the source has as defined from the *HST* data, and the PSFs centroids were placed at the positions of $K_{\rm s}$-band centroids used as priors, allowing a shift in both the X and Y axes that turns out to be <1 pixel from the initial positions (the IRAC image pixel scale is $0.''6\,{\rm pixel}^{-1}$). The uncertainties in the photometry due to the deblending were calculated by performing a number of realizations varying the centroid coordinates randomly within 1 pixel of the best-fit centroid and fixing those coordinates for each realization. Additionally, we checked for detections in the IRAC 5.8 and 8.0 μm bands from the S-COSMOS survey (Sanders et al. 2007), but the sources are not detected at the required 5σ level (upper limits are included in Figure 2).

We fitted the resulting 13-band SEDs (g to 4.5 μm, including the three *HST* bands) using LePHARE (Arnouts et al. 1999; Ilbert et al. 2006). We adopted Bruzual & Charlot (2003) stellar population synthesis models with emission lines to account for contamination from Hα, which at the redshift probed in this work is redshifted into the IRAC 3.6 μm band. A Chabrier (2003) IMF, exponentially declining star formation histories (SFHs), and a Calzetti et al. (2000) dust law were assumed. We explored a large parameter grid in terms of SFH e-folding times (0.1–30 Gyr), extinction ($0 < A_V < 5$), stellar age (1 Myr–age of the universe at the source redshift), and metallicity ($Z = 0.004$, 0.008, and 0.02, i.e., solar). The redshift was fixed to the spectroscopic redshift, if available, or to the photometric redshift if not (see Table 3). In Figure 2, we show the derived SEDs, with the fitted models being in good agreement with the data.

4. Dust Absorption and Emission

4.1. Spatially Resolved UV Slopes

At the redshift of the galaxies, the three *HST* bands trace the rest-frame UV continuum. This makes it possible to directly determine their spatially resolved UV slopes (β).

In Figure 3, we present β maps constructed by fitting a linear slope to pixels that have ${\rm S/N} > 2$ detections in at least two smoothed images (see Section 2.5). The 1σ uncertainty maps (inserts) were constructed by computing β-values in $\sim$10,000 realizations of the data, varying in each realization the measured pixel flux values within their uncertainties. Note that the pixel size is $0.''06$, but the PSF FWHM is $0.''18$. Consequently, spatially independent regions are those separated by at least 3 pixels. Since the UV slope maps were obtained using at least two detections in the *HST* bands, we see more clearly the presence of faint companions toward the north in AK03, AzTEC1, AzTEC5, and J1000+0234, as mentioned in Section 3.

In general, the objects present blue UV slopes, but the values are not homogeneous over the extent of the galaxies. The color gradients could be caused by structure in the distribution of dust, stellar age, or metallicity. The relative importance of these cannot be disentangled from the available data, but we expect a patchy dust distribution to be the dominant cause. However, as most of the extent of the rest-frame UV emission is not detected in our ALMA observations, revealing the underlying dust structure in emission would require deeper observations.

The rest-frame FIR dust emission is in all cases associated with the reddest components. These components show evidence of gradients in their UV slopes. AK03-S is redder toward the northeast and bluer at the southwest. J1000+0234-N has an extended redder feature at the northeast. Vd-17871-N is slightly redder toward the southwest and bluer toward the

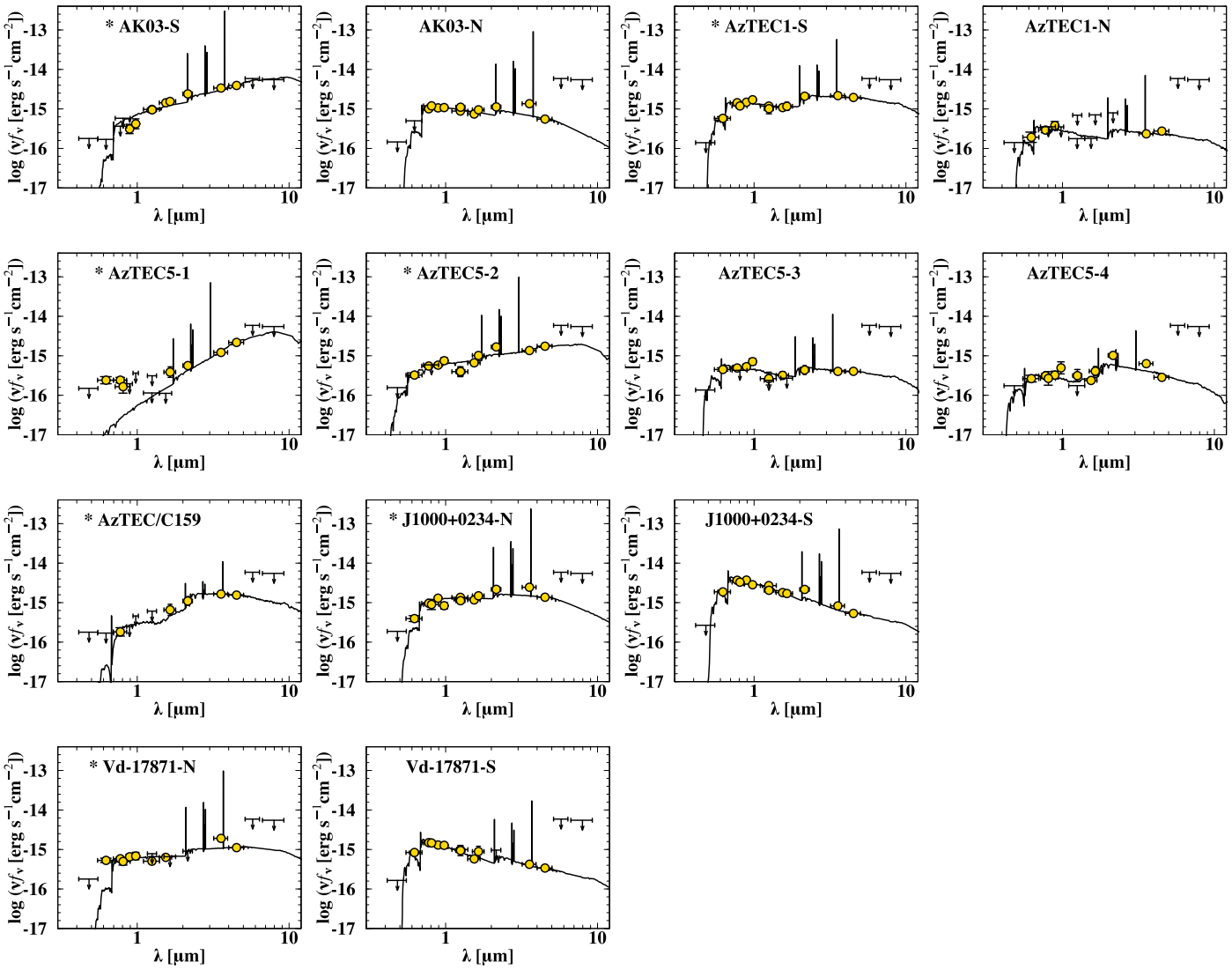

Figure 2. SED and best fit for the different stellar components of each object in the sample. Wavelengths are in the observer frame. Arrows indicate 3σ upper limits (5σ for the *Spitzer* bands). Component names preceded by a star refer to those with an ALMA counterpart.

northeast. In AzTEC1-N, the red-to-blue gradient goes along the north–south axis. These color gradients may be due to a star formation gradient with higher dust content toward the redder areas. Another possibility could be close mergers between red and blue galaxies.

In AK03-S, two close FIR peaks are detected. At the current resolution and sensitivity and without dynamical information, we cannot determine whether these are part of a larger dynamical structure like a clumpy disk or remnants of a past interaction/merger. Note that in AzTEC5, we were unable to constrain the resolved UV slope of AzTEC5-1, since it is only detected in F814W, suggesting an extremely high extinction with strong rest-frame FIR emission but also a very blue rest-frame UV component.

The bluer components in all five systems remain undetected in the ALMA continuum. This indicates less dusty star formation.

Spatially integrated values for the UV slopes (see Table 3) show a median and median absolute deviation of $\beta = -0.59 \pm 0.57$ for the components associated with the ALMA continuum emission (namely, AK03-S, AzTEC1-S, AzTEC5-2, J1000+0234-N, and Vd-17871-N and excluding the AzTEC5-1 and AzTEC/C159 upper limits). The rest of the components are bluer, with $\beta = -1.73 \pm 0.54$, consistent with estimates of Lyman break galaxies (LBGs) at similar redshift (e.g., Bouwens et al. 2009; Castellano et al. 2012; Finkelstein et al. 2012). By performing the photometry over larger apertures, enclosing all the components per source, we derive $\beta = -0.91 \pm 0.85$, which is in between the derived values for the red and blue components.

Having identified which UV components are associated with the dust continuum emission, we can relate the SFR in the IR (SFR_{IR}), tracing the obscured star formation, with that in the UV (SFR_{UV}), probing the unobscured star formation. The former was obtained from the FIR SEDs presented in Smolčić et al. (2015; Toft et al. 2014 for AzTEC5) covering 100 μm–1.1 mm, updated with new 850 μm fluxes from the S2COSMOS/SCUBA2 survey (J. M. Simpson et al. 2018, in preparation). The procedure is as follows. The FIR SED is modeled using the Draine & Li (2007) dust model (DL07; e.g., Magdis et al. 2012, 2017; Berta et al. 2016), L_{IR} is calculated by integrating the best fit to the SED in the range 8–1000 μm, and the SFR_{IR} is obtained using the L_{IR}-to-SFR_{IR} conversion from Kennicutt (1998) for a Chabrier IMF. The SFR_{UV} was calculated employing the Salim et al.

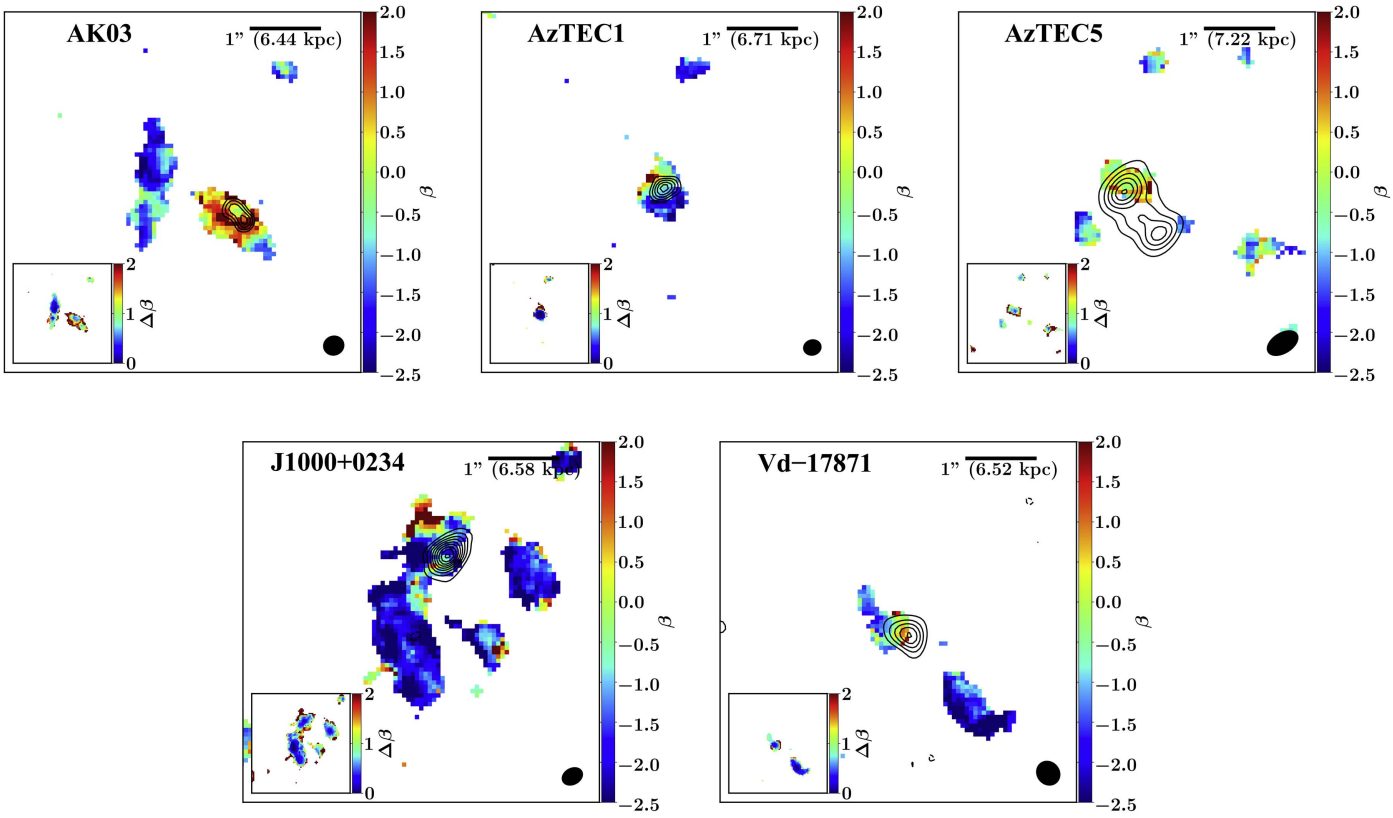

Figure 3. UV continuum slope maps of the five sources observed with *HST*. ALMA band 7 (∼870 μm) contours are overlaid starting at $\pm 3\sigma$ in steps of 1σ (AK03 and AzTEC1) or 3σ (AzTEC5, J1000+0234, and Vd-17871). The error map is shown in the bottom left corner, and the ALMA beam size is in the bottom right corner of each panel. North is up, east is to the left, and the images have a size of $5'' \times 5''$.

(2007) prescription that relates $L_{\rm UV}$ to $\rm SFR_{UV}$ for a Chabrier IMF. Note that $\rm SFR_{UV}$ derived this way corresponds to the observed value, i.e., not corrected from extinction. The total SFR can be accounted for by adding both IR and UV estimates ($\rm SFR_{IR+UV}$). Not surprisingly, the star formation is dominated by $\rm SFR_{IR}$, with $\rm SFR_{UV}$ only contributing at the level of 2%–20% to the total SFR ($\rm SFR_{IR+UV}$), in agreement with other previous works comparing obscured and unobscured star formation in starburst galaxies (e.g., Puglisi et al. 2017) and galaxies with similar stellar mass (e.g., Whitaker et al. 2017).

In relation to the $L_{\rm IR}$ and $\rm SFR_{IR}$ estimates, it is important to consider whether an important fraction of the IR emission could be related to active galactic nucleus (AGN) activity. As reported in Smolčić et al. (2015), none of the sources are detected in the X-ray catalog in the COSMOS field (*Chandra* COSMOS Legacy Survey; Civano et al. 2016; Marchesi et al. 2016). In terms of the radio emission, Smolčić et al. (2015) studied the IR–radio correlation of the sample, which shows a discrepancy when compared with low-redshift star-forming galaxies due to a mild radio excess. This excess would be in line with studies showing an evolving IR–radio ratio depending on the age of the starburst. In any case, while many SMGs host AGNs, their $L_{\rm IR}$ is dominated by star formation, with the AGN contribution being <33% (e.g., Pope et al. 2008; Riechers et al. 2014b). This translates into a maximum overestimation in the $\rm SFR_{IR}$ of 33%, below the $\rm SFR_{IR+UV}$ sample scatter.

4.2. FIR Sizes

We measured the sizes of the rest-frame FIR dust continuum emission by modeling the ALMA continuum images using GALFIT. Sérsic and PSF profiles were fitted to compare both resolved and unresolved modeling of the objects. The only object that was better fitted by a point source than a Sérsic model (and thus unresolved) is AK03. For this galaxy, we derived an upper limit on the size from the PSF.

For the rest of the galaxies, we fitted models with the Sérsic index fixed to $n = 0.5$, 1, and 4, corresponding to a Gaussian, exponential disk, and de Vaucouleurs profiles, respectively, and also leaving the index free. The size of the emitting regions was obtained through the effective radius of the models (r_e). We cannot constrain which Sérsic index better explains the data at the current resolution and S/N. From higher-resolution observations, Hodge et al. (2016) found a median Sérsic index of $n = 0.9 \pm 0.2$ for a sample of 15 SMGs and concluded that the dust emission follows an exponential disk profile. Motivated by this, we fixed $n = 1$ to report the rest-frame FIR sizes for our sample in Table 4. We also performed fits varying the axis ratio (b/a) and found that no particular value with $b/a \geqslant 0.3$ fitted the data better than others, so we fixed it to the circular value $b/a = 1$. We take into account the possible systematic errors associated with the assumed Sérsic index and axis ratio in the listed effective radii errors. These were computed by adding in quadrature the statistical uncertainty from GALFIT for the circular disk model and the difference between this model and the full range of models with varying n and b/a. Therefore, the uncertainties conservatively account for the inability of the data to robustly constrain the detailed shape of the surface brightness profiles. We note that the ALMA continuum fluxes are consistent with the 850 μm fluxes from the S2COSMOS/SCUBA2 survey (J. M. Simpson

Table 4
Rest-frame FIR Sizes

Source Name[a]	r_e^{GALFIT} (pc)	r_e^{GALFIT} (arcsec)	$r_e^{UVMULTIFIT}$ (pc)	$r_e^{UVMULTIFIT}$ (arcsec)	Σ_{SFR}[b] ($M_\odot$ yr^{-1} kpc^{-2})	Σ_{dust}[b] (10^9 $M_\odot$ kpc^{-2})
AK03-S[c]	<520	<0.08	⋯	⋯	>3.4	>1.4
⋯	<520	<0.08	⋯	⋯	>3.8	>1.6
AzTEC1-S	900^{+480}_{-290}	$0.13^{+0.07}_{-0.04}$	940 ± 70	0.14 ± 0.01	480^{+540}_{-340}	$1.0^{+1.1}_{-0.7}$
AzTEC5-1[d]	300^{+90}_{-130}	$0.04^{+0.01}_{-0.02}$	⋯	⋯	1260^{+870}_{-1200}	$1.7^{+1.1}_{-1.5}$
⋯	560^{+120}_{-360}	$0.08^{+0.02}_{-0.05}$	⋯	⋯	250^{+330}_{-140}	$0.33^{+0.16}_{-0.43}$
AzTEC5-2	700^{+180}_{-390}	$0.10^{+0.03}_{-0.05}$	⋯	⋯	390^{+240}_{-440}	$0.51^{+0.30}_{-0.58}$
AzTEC/C159	460^{+60}_{-240}	$0.07^{+0.01}_{-0.04}$	590 ± 70	0.09 ± 0.01	570^{+220}_{-610}	$1.9^{+2.0}_{-0.7}$
J1000+0234-N	700^{+120}_{-100}	$0.11^{+0.02}_{-0.02}$	660 ± 70	0.10 ± 0.01	150^{+380}_{-110}	$1.6^{+3.5}_{-1.2}$
Vd-17871-N	370^{+80}_{-210}	$0.06^{+0.01}_{-0.03}$	650 ± 70	0.10 ± 0.01	1300^{+670}_{-1500}	$5.8^{+4.2}_{-7.7}$

Notes.
[a] Names refer to the stellar component associated with the FIR emission.
[b] Defined as $\Sigma_{SFR} = 0.5SFR/\pi\ (r_{e,circ}^{GALFIT})^2$ and $\Sigma_{dust} = 0.5M_{dust}/\pi\ (r_{e,circ}^{GALFIT})^2$.
[c] Limits from the PSF referring to each one of the two emitting regions.
[d] The three values of AzTEC5 allude to the three resolved emitting regions from west to east.

et al. 2018, in preparation); thus, there is no evidence for resolved-out or missing flux that could affect the size estimates.

Finally, we cross-checked the results, analyzing the data directly in the (u, v) plane employing UVMULTIFIT (Martí-Vidal et al. 2014) following the procedure described in Fujimoto et al. (2017). In this case, for a direct comparison with the GALFIT image-plane fits, we also assumed a circular disk model (to obtain secure results, we omit AK03 and AzTEC5 for this comparison, as they show two and three components, respectively, in our ALMA continuum images). We find that these estimates are in agreement with the results derived in the reconstructed images using GALFIT (see Table 4). In the following, we use the estimates derived from GALFIT for further calculations.

The median and median absolute deviation of the size estimate for our sample are then $r_e = 0.70 \pm 0.29$ kpc at ∼870 μm, which corresponds to ∼160 μm rest frame at $z = 4.5$ (excluding the AK03 upper limits and only considering the brightest peak in AzTEC5, associated with AzTEC5-2). This result is in good agreement with that of Ikarashi et al. (2015), who found similar compact sizes of $r_e = 0.67^{+0.13}_{-0.14}$ kpc for a sample of 13 1.1 mm selected SMGs at a comparable redshift $3 < z < 6$. Oteo et al. (2017) presented an average value of $r_e = 0.91 \pm 0.26$ kpc (converting the reported FWHM into a circularized effective radius) in a sample of 44 DSFGs at $z \sim 4$–6 observed at ∼870 μm and selected as *Herschel* 500 μm risers (SED rise from 250 to 500 μm). On the other hand, the typical sizes derived for SMGs at a median redshift of $z \sim 2.5$ were reported to be $r_e = 1.8 \pm 0.2$ kpc from Hodge et al. (2016) and $r_e = 1.2 \pm 0.1$ kpc from Simpson et al. (2015), both targeting ∼870 μm. This suggests that SMGs may be more compact at $z > 3$ than at $z < 3$ (e.g., Fujimoto et al. 2017; Oteo et al. 2017). Other individual sources at $z > 4$ also point toward very compact dust continuum emission (e.g., Riechers et al. 2013, 2014a; Díaz-Santos et al. 2016) and pairs of compact interacting starburst galaxies detected in gas and dust continuum, which suggests a gas-rich major merger (e.g., Oteo et al. 2016; Riechers et al. 2017). Spilker et al. (2016) found no evidence for a difference in the size distribution of lensed DSFGs compared to unlensed samples from a sample of 47 DSFGs at $z = 1.9$–5.7. Our results are also similar to the compact morphologies of local ultra-luminous infrared galaxies (ULIRGs; $r_e = 0.5$ kpc; Lutz et al. 2016) at 70 μm rest frame. We note that caution should be exercised when comparing samples tracing different rest-frame FIR wavelengths and based on different selection methods. Another caveat for a fair comparison is the stellar mass, since more massive galaxies are typically larger (e.g., van der Wel et al. 2014).

From the SFR_{IR} obtained for these sources (see Table 3) and their rest-frame FIR sizes, we calculated the SFR surface density ($\Sigma_{SFR} = 0.5SFR/\pi r_{e,circ}^2$; see Table 4). Ranging from $\Sigma_{SFR} = 150$ to 1300 $M_\odot$ yr^{-1} kpc^{-2} (excluding AK03 lower limits), the most extreme cases are AzTEC1, AzTEC5-1, and Vd-17871-N, but the last two are poorly constrained due to the large uncertainty on their sizes. At such extreme values, they are candidates for Eddington-limited starbursts ($\Sigma_{SFR} \sim 1000\ M_\odot$ yr^{-1} kpc^{-2}; Andrews & Thompson 2011; Simpson et al. 2015).

4.3. UV/FIR Spatial Disconnection

The dust masses derived for this sample are very high at $\sim 10^9$ $M_\odot$ (see Table 3). Dust masses are a free parameter in the DL07 model employed, controlling the normalization of the SED. In terms of the dust opacity, DL07 assumes optically thin dust ($\tau << 1$) at all wavelengths (e.g., Magdis et al. 2012, 2017; Berta et al. 2016). Very high dust masses combined with the small sizes derived for the dust-emitting regions implies very high dust mass surface densities ($\Sigma_{dust} = 0.5M_{dust}/\pi r_{e,circ}^2$) with values in the range $\Sigma_{dust} = 0.33$–$5.8 \times 10^9\ M_\odot$ kpc^{-2} (see Table 4) and, consequently, very high extinction.

We calculated the expected extinction assuming that the dust is distributed in a sheet with uniform density. We inferred the mean extinction from the dust mass surface density–to–extinction ratio (Σ_{dust}/A_V). To calculate Σ_{dust}/A_V, we assumed a gas-to-dust mass ratio (GDR) appropriate for SMGs of GDR = 90 (Swinbank et al. 2014) and the gas surface number density–to–extinction ratio $N_H/A_V = 2.2 \times 10^{21}$ cm^{-2} mag^{-1} (Watson 2011). Therefore, $\Sigma_{dust}/A_V = (N_H/A_V) \cdot m_H/\mathrm{GDR} = 2.44\ M_\odot$ pc^{-2} mag^{-1}. With this number, the mean extinction is $\langle A_V \rangle = \Sigma_{dust}/2.44$. The values for our sample are extreme $\langle A_V \rangle = 130$–2400 mag, even when the numbers are halved to account for the dust behind the sources (see also Simpson et al. 2017).

Comparing Figures 1 and 3, we see that while the dust emission is always associated with the reddest (likely most dust-extincted) component, in most cases it is not centered on the reddest part of that component (with the possible exception

of Vd-17871). This suggests that the extinction seen in emission and absorption is disconnected, consistent with the expected extreme A_V, which implies that no emission can escape at any wavelength.

The fact that we do see blue UV emission at the peak of the dust emission suggests that a fraction of the light is able to escape due to a clumpy dust distribution and/or that the dust and stars are seen in different projections; e.g., the stars responsible for the UV emission could be in front of the dusty starbursts.

In any case, it is clear that the rest-frame UV and FIR emissions are spatially disconnected and originate from a different physical region. This implies that the dust as seen in absorption from the UV slope inhomogeneities in Figure 3 is not tracing the dust seen in emission from the ALMA continuum.

4.4. IRX–β Plane

The IR-to-UV luminosity ratio, commonly referred to as IR excess (IRX $= L_{\rm IR}/L_{\rm UV}$), is known to correlate with the UV continuum slope (β). This so-called Meurer relation (Meurer et al. 1999, hereafter M99) is well established for normal star-forming galaxies (e.g., Overzier et al. 2011; Takeuchi et al. 2012; Casey et al. 2014b). Its origin is thought to be that galaxies get redder as the dust absorbs the rest-frame UV emission and reradiates it at IR wavelengths. For galaxies on the relation, the amount of dust absorption can thus be directly inferred from the UV slope. Therefore, in the absence of FIR data, the relation can be used to obtain a total extinction-corrected SFR from UV data (e.g., Bouwens et al. 2009). Furthermore, this relation physically motivates energy balance codes that require that dust extinction inferred from rest-frame UV–optical SED fits must match the observed emission measured at IR wavelengths (e.g., da Cunha et al. 2008).

Spatially unresolved observations have shown that DSFGs do not follow the M99 relation (e.g., Buat et al. 2005; Howell et al. 2010; Casey et al. 2014b). An excess of dust and UV/FIR decoupling have both been suggested as a possible origin of the offsets by Howell et al. (2010), who showed that the deviation from the nominal M99 relation (ΔIRX) increases with $L_{\rm IR}$ but does not correlate with $L_{\rm UV}$. Following this argument, the authors postulated that a concentration parameter might correlate with ΔIRX as an indicator of the decoupled UV/FIR. Casey et al. (2014b) reinforced these results, showing that the deviation from the M99 relation increases with $L_{\rm IR}$ above a threshold of $\log(L_{\rm IR}/L_\odot) > 11.0$. Faisst et al. (2017a) proposed that the blue colors of sources with high IRX values could be due to holes in the dust cover, tidally stripped young stars, or faint blue satellite galaxies. In addition, simulations propose recent star formation in the outskirts and low optical depths in UV-bright regions as plausible explanations of the offset (Safarzadeh et al. 2017; Narayanan et al. 2018). Simple models placing a dust screen in front of a starburst have been studied to provide a detailed explanation of all the possible effects that might lead to a deviation in the IRX–β plane (Popping et al. 2017b).

The sample studied here has IR luminosities in the range $\log(L_{\rm IR}/L_\odot) = 12.1$–$13.4$, above the mentioned threshold $\log(L_{\rm IR}/L_\odot) > 11.0$, and the spatially resolved rest-frame UV/FIR data make it possible to study the origin of the DSFG offsets in the IRX–β plane (see Figure 4).

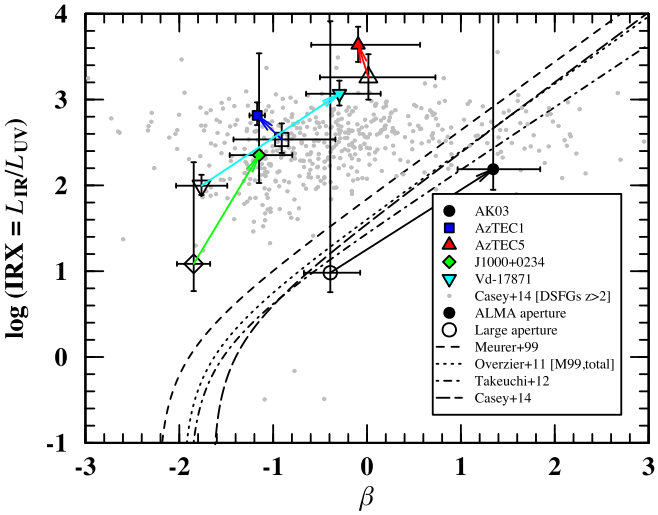

Figure 4. IRX–β plane. Small filled symbols indicate *HST* photometry performed over the region above the 3σ contour in the ALMA image. Large open symbols refer to *HST* photometry performed over a large aperture enclosing all the components of each source. Both small and large symbols are linked with an arrow of the color associated with each object. Small gray dots indicate the Casey et al. (2014b) sample of DSFGs at $z > 2$. IRX–β relations from the literature include Meurer et al. (1999; dashed line); the corrected M99 relation, referred to as "M99, total" in Overzier et al. (2011; dotted line); Takeuchi et al. (2012; dash-dotted line); and Casey et al. (2014b; long-dashed line). Our sample does not follow the M99 relation, which, together with the rest-frame UV and FIR morphologies, suggests that the UV and FIR emissions of DSFGs are spatially disconnected.

To confirm that the galaxies in this sample are representative of previous DSFG studies in spatially unresolved data, we first derived UV and IR luminosities in large apertures enclosing all the components of each source. In Figure 4, these measurements are plotted as large open symbols, confirming that the sample does not follow the M99 relation and is located in the same region as previous spatially unresolved measurements for DSFGs (e.g., Casey et al. 2014a at $z > 2$). Second, we take advantage of the spatial resolution to pinpoint the origin of the FIR emission and recalculate the UV luminosity in smaller apertures defined by the 3σ contour in the ALMA images (ALMA apertures). In this case, both the *HST* and ALMA images were PSF-matched as described in Section 2.4.

In Figure 4, we plot the sample of DSFGs at $z > 2$ from Casey et al. (2014b) for comparison. Note that this study employed similar methods to obtain $L_{\rm IR}$, $L_{\rm UV}$, and the UV slopes as we did: $L_{\rm IR}$ by integrating over the wavelength range 8–1000 μm and using a single temperature modified graybody plus mid-IR power law, which properly accounts for the warm dust contribution as the DL07 dust model; $L_{\rm UV}$ by interpolating the observed photometry to rest-frame 1600 Å; and the UV slopes by fitting a power law to the photometry, which is equivalent to our linear fit in magnitude space. Additionally, we include other IRX–β relations from the literature: the original M99 and follow-up corrections (e.g., Overzier et al. 2011; Takeuchi et al. 2012), although the methodology they followed to obtain the quantities shown in the IRX–β diagram slightly differs from that of Casey et al. (2014b) and us.

All of the galaxies have higher IRX in the ALMA aperture than in the large aperture. This is expected from their smaller extent in the rest-frame FIR compared to that in the rest-frame UV, which effectively lowers the $L_{\rm UV}$ contribution to the

L_{IR}/L_{UV} ratio. Furthermore, three of the galaxies have redder UV slopes and two have similar UV slopes in the ALMA apertures compared with the large apertures. Again, this can be understood as a result of removing the contribution from the extended irregular UV features and companion satellite galaxies that appear bluer than the dust-emitting region detected in ALMA. These results agree with the model proposed in Faisst et al. (2017a) to explain the blue colors of DSFGs with high IRX.

On the other hand, even after accounting for the correction that implies going from the large to the ALMA aperture, our sample does not follow the M99 relation and lies 1.75 dex (median) above it. However, while the rest-frame FIR dust continuum emission is associated with the reddest component in the mergers, it is generally not centered on the reddest part of the component, and the component is too blue to be consistent with a physical connection between the dust seen in emission and absorption, suggesting that the UV and FIR emissions of DSFGs are spatially disconnected.

This provides morphological and geometrical evidence for the origin of the DSFG offsets from the M99 relation (see also Chen et al. 2017) being consistent with the extreme extinction expected from the compact and intense dust emission for this sample (see Section 4.3), implying that UV emission should be expected not to escape the starbursts.

A possible scenario for the origin of the UV and FIR emissions could be a patchy dust distribution causing some of the UV to be completely extincted and some to leak relatively unextincted, in a similar way as proposed by the holes in the dust cover by Faisst et al. (2017a).

The UV/FIR lack of spatial coincidence has important implications for energy balance codes, as noted by Hodge et al. (2016), where the detected stellar light will have no information about the obscured starburst (Simpson et al. 2015).

Therefore, the results here support that IRX and β are unrelated for such FIR-bright sources and that extinction-correction prescriptions based on the nominal IRX–β relation are inappropiate for DSFGs.

In Section 4.1, we interpreted the UV slope differences over the source extent as variations in the dust content not detected in emission in the ALMA observations. It is possible that this regime of star formation is compatible with the M99 relation. In order to check this, we calculated the expected L_{IR} below the 3σ dust continuum detection limit over the components detected in the rest-frame UV for each source by rescaling their FIR SEDs (Toft et al. 2014; Smolčić et al. 2015). The resulting upper limits lie above the M99 relation for all cases, not being useful for putting constraints about whether these galaxies follow M99 or lie above or below it, a subject of main focus in current studies (e.g., Capak et al. 2015; Barisic et al. 2017; Faisst et al. 2017a; Fudamoto et al. 2017).

5. Stellar Masses and Merger Ratios

5.1. What Triggers $z > 4$ Starbursts?

Major mergers between gas-rich galaxies are often assumed to be the triggering mechanism for starburst galaxies, as local universe IR-luminous galaxies are exclusively associated with major mergers with $L_{IR} > 10^{11.5}\ L_{\odot}$ (e.g., Sanders & Mirabel 1996). The multiplicity of close, approximately equally bright galaxies in the *HST* images studied here would naively support a similar triggering mechanism at $z > 4$. However, as the images trace the rest-frame UV, a stellar mass analysis of the individual merging components is needed to test this picture.

In Table 3, we list the stellar masses of the stellar components of each system derived from the SED fits described in Section 3.2. Also listed is the stellar mass ratio relative to the most massive component in the system ($M_{*,prim}$).

The median stellar mass of the most massive component is $\log(M_*/M_{\odot}) = 10.49 \pm 0.32$ (where the uncertainty is the median absolute deviation). For the remaining less-massive components, the median is $\log(M_*/M_{\odot}) = 9.56 \pm 0.10$. A stellar mass ratio of 1:3–4 is often adopted to distinguish between major and minor mergers (e.g., Conselice et al. 2003; Tacconi et al. 2008; Kaviraj et al. 2009; Lotz et al. 2011; Man et al. 2016). Adopting this definition, AzTEC5 is formally classified as a major merger, with a stellar mass ratio for the two most massive components (AzTEC5-1 and AzTEC5-2) of $M_*/M_{*,prim} = 3.0$. Vd-17871 could be classified as a major or minor merger, depending on the exact distinction ratio ($M_*/M_{*,prim} = 3.5$). The rest of the systems are consistent with undergoing at least one minor merger (including AzTEC5, which might undergo minor merging with AzTEC5-3 and AzTEC5-4). Furthermore, it is important to note that regardless of the precise distinction between major and minor mergers, the components detected in dust continuum with ALMA are undergoing starbursts with SFRs that overwhelm those of the companions; therefore, the stellar mass ratios are expected to decrease. Taking this into account, all systems could be classified as minor mergers (except AzTEC5-1 and AzTEC5-2, both starbursting systems).

In addition to the components that were bright enough to estimate stellar masses, AK03, AzTEC5, and J1000+0234 present additional low-S/N companions detected in one or more of the *HST* images (marked with arrows in Figure 1), which may be additional minor merger components if they are at the same redshift. The residuals in the modeling of the *Spitzer*/IRAC images do not show significant detections at their positions; thus, they must be less massive than the detected companions. In fact, the *HST* images display $2 < S/N < 3$ potential additional low-mass components in the case of F814W particularly, as expected if they are small, blue star-forming galaxies. If their redshifts are confirmed, it will be further evidence for the starbursts in $z \sim 4.5$ SMGs being triggered by multiple minor mergers, a picture consistent with living in overdense environments (e.g., Blain et al. 2004; Smolčić et al. 2017). Indeed, Smolčić et al. (2017) showed evidence that AzTEC1, AzTEC5, J1000+0234, and Vd-17871 have statistically significant small-scale overdensities.

Note, however, that these results do not rule out that major mergers played a role in triggering these starbursts if they have already coalesced or are so close that they are not resolved in the *HST* and ALMA data. Indeed, the multiple FIR peaks in AK03 and AzTEC5 and the color gradients observed in the most massive components of the systems (most prominently in AzTEC1, J1000+0234, and Vd-17871) are consistent with such a picture.

5.2. Comparison to Previous Stellar Mass Estimates

Previous estimates of the stellar mass of the galaxies in this sample, derived using MAGPHYS (da Cunha et al. 2008), led to a median value of $\log(M_*/M_{\odot}) = 10.92 \pm 0.13$ (Toft et al. 2014; Smolčić et al. 2015). This is ~0.4 dex higher than

our derived median value for the most massive component. Adding up all the components per source, the median total stellar mass would be slightly higher, $\log(M_*/M_\odot) = 10.63 \pm 0.11$, but still $\sim$0.3 dex lower than the previous estimates for this sample. Recent results from Miettinen et al. (2017), also employing MAGPHYS, are also systematically higher by at least 0.3 dex for the sources in common with our sample (AzTEC1, AzTEC5, and J1000+0234). Such systematic discrepancies are consistent with the expected overestimation of MAGPHYS-derived stellar masses and slight underestimation of exponentially declining models employed here, according to Michałowski et al. (2014) SMG stellar mass studies from simulated data sets.

We also compared our stellar mass estimates with those listed in the 3D-*HST* survey catalog (Brammer et al. 2012; Skelton et al. 2014; Momcheva et al. 2016) for the sources covered in the CANDELS fields (e.g., AK03 and AzTEC5) and the COSMOS2015 catalog (Laigle et al. 2016). In general, the catalogs successfully extract the majority of the components for these complex objects and list photometric redshifts consistent with the available spectroscopic redshifts (see Table 3). However, for a subset, we found significant discrepancies in the derived stellar masses. The discrepancy might be due to the different approach in the photometry measurements. While we measured fluxes in apertures carefully chosen to minimize the effect of blending and applied aperture corrections, COSMOS2015 employs automated PSF-matched photometry, which can be more contaminated by blending of close objects.

Furthermore, J1000+0234-N is not in the COSMOS2015 catalog, and the bulk of its stellar mass is associated with J1000+0234-S (likely due to a mismatch between the *Spitzer*/IRAC and optical/near-IR data). AzTEC/C159 is also missing from the catalog, due to its extreme faintness in the optical/near-IR. Similarly, there is no entry corresponding to the location of AzTEC5-1 in either 3D-*HST* or COSMOS2015. The absence and misidentifications of massive and optically faint sources could affect the photometry and, thus, the stellar mass estimates. It could also affect the stellar mass functions at high redshifts (e.g., Davidzon et al. 2017).

J1000+0234 is also present in the recent work by Brisbin et al. (2017), and the assigned shorter-wavelength counterpart to the ALMA detection is also J1000+0234-S, since J1000+0234-N remains undetected. This indicates that significant offsets between sub-mm/radio sources and UV/optical/near-IR counterparts could indeed be due to the presence of multiple blended, and perhaps merging, components if the depth and resolution of the data are not enough to detect all those components (provided a good relative astrometry between the different instruments).

Compared with previous estimates of the average stellar masses of SMGs, our results are in line with studies indicating that most SMGs have $M_* < 10^{11}\ M_\odot$ (e.g., Hainline et al. 2011; Wardlow et al. 2011; Casey et al. 2013; Simpson et al. 2014). Other studies also report higher values of $M_* > 10^{11}\ M_\odot$ for $z \sim 4.5$ sources (Michałowski et al. 2010, 2012, 2017). The median stellar mass of the satellite galaxies is consistent with estimates for faint LBGs at similar redshifts (Magdis et al. 2010).

5.3. Stellar Mass Uncertainties and Caveats

Stellar masses of highly obscured starburst galaxies are notoriously difficult to estimate. In this work, we took advantage of high-resolution *HST* imaging to identify the positions of multiple stellar components in the systems, which in turn was used to deblend the rest-frame optical *Spitzer*/IRAC fluxes that are tracing the stellar mass available for these high-redshift systems. However, our stellar mass estimates are potentially subject to a number of additional systematic uncertainties.

One caveat is that some of the components lack spectroscopic confirmation. That is the case for AK03-S, AzTEC1-N, and all components of AzTEC5. When possible, we assumed that these components were at the same redshift as their spectroscopically confirmed companions. For AK03-S, Smolčić et al. (2015) found $z_{\rm phot} = 4.40 \pm 0.10$ or 4.65 ± 0.10, depending on the template used. Therefore, the two components are likely at the same redshift. AzTEC1-N is a very faint component with S/N < 3 in all *HST* bands, but it is detected above this threshold in the HSC *r*, *i*, and *z* bands and the IRAC bands, where the residuals from AzTEC1-S fitting showed that there is indeed a secondary component toward the north. We derived a photometric redshift consistent with being at the same redshift as AzTEC1-S within the uncertainties. Its probability distribution peaks at $3.77^{+0.32}_{-0.22}$ (where the uncertainties are the 1σ percentiles of the maximum-likelihood distribution), being not null in the redshift range $3.2 < z < 4.7$. In the case of AzTEC5, none of the components have spectroscopic redshifts, but the 3D-*HST* survey catalog (Brammer et al. 2012; Skelton et al. 2014; Momcheva et al. 2016) lists $z_{\rm phot} = 3.63^{+0.14}_{-0.15}$ for AzTEC5-2, $z_{\rm phot} = 4.02^{+0.08}_{-0.08}$ for AzTEC5-3, and $z_{\rm phot} = 3.66^{+0.40}_{-0.43}$ for AzTEC5-4. Therefore, it seems plausible that all components in AzTEC5 lie at the same redshift within the uncertainties.

Another caveat in the stellar mass estimates comes from the assumptions made in the SED fits. Michałowski et al. (2014) studied the importance of the assumed SFHs (see also Hainline et al. 2011) over several SED fitting codes, concluding that the exponentially declining SFHs used here are able to recover the stellar masses of their simulated SMGs with slight underestimation and significant scatter. Regardless of the model employed, the derived photometry and the color of the sources already indicate that there is a component more massive than the other. The most massive components have higher IRAC fluxes, and they are also redder than their fainter IRAC companions.

Given the extreme dust mass surface densities derived for this sample (see Table 4), if the stars formed in situ in the starburst that created the dust, it is possible that some stellar mass is so obscured that it is not detectable even by IRAC and, thus, not accounted for in the SED fitting. Higher spatial resolution rest-frame FIR continuum observations would be needed to disentangle the underlying structure of the dust-emitting region and measure its degree of homogeneity or clumpiness. This could reveal how much of the stellar light is completely obscured beneath the dust and the implied systematic error in the derived stellar masses. To estimate how big this effect could be, using the empirical dust–to–stellar mass ratio (DTS) for local ULIRGs in Calura et al. (2017) $\log{\rm DTS} = -2.83$, the median stellar mass of this sample would increase to $\log(M_*/M_\odot) \sim 11.6$. However, assuming the ratio from simulations in Popping et al. (2017c), $\log{\rm DTS} \sim -1.8$, the effect would not be that significant, increasing to $\log(M_*/M_\odot) \sim 10.9$.

Over the last decade, several studies have uncovered a tight correlation between the SFR and the stellar mass of

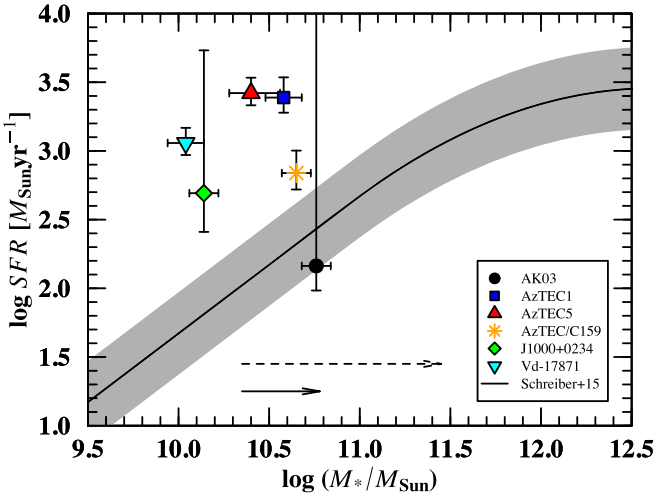

Figure 5. The SFR–M_* plane. Our sample (colored symbols) lies above the MS of star-forming galaxies as defined by Schreiber et al. (2015; plotted at $z = 4.5$ for reference and converted from Salpeter to Chabrier IMF). A 0.3 dex (2 times) scatter around the MS is represented by the gray shaded region. The bottom arrows indicate the estimated increase in the derived stellar masses if a fraction is obscured by the dust (log DTS ~ -1.8 from Popping et al. 2017c, solid arrow; log DTS $= -2.83$ from Calura et al. 2017, dashed arrow).

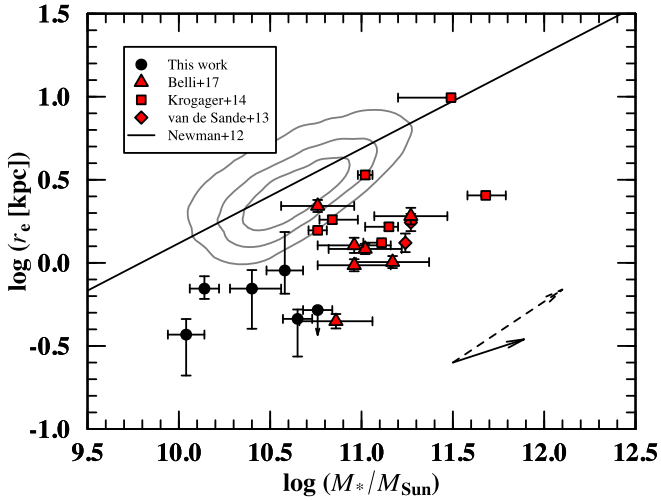

Figure 6. Stellar mass–size plane location of the SMG sample in this work (black filled circles), along with $z \sim 2$ cQGs (red filled symbols) from van de Sande et al. (2013; diamonds), Krogager et al. (2014; squares), and Belli et al. (2017; triangles). The black solid arrow at the bottom right indicates the expected evolution of the SMG sample, accounting for the stellar mass growth through the derived SFR_{IR+UV} over a dusty circle of 42 Myr and minor merger contribution and in size via minor mergers. The dashed arrow indicates the predicted evolution from a potential scenario with longer depletion timescales of 100 Myr and larger sizes assuming a [C II] size proxy for the effective star-forming region. For comparison, the local mass–size relation from Newman et al. (2012) is shown as a solid line, along with SDSS local massive quiescent galaxies as gray contours (Shen et al. 2003). All plotted data were converted to a concordance cosmology [Ω_Λ, Ω_M, h] = [0.7, 0.3, 0.7] and Chabrier IMF when needed.

star-forming galaxies, the so-called main sequence (MS) of star formation (e.g., Daddi et al. 2007; Elbaz et al. 2007; Noeske et al. 2007). Strong outliers to the MS are present at all redshifts, and this is often used as a formal definition of starburst galaxies. These systems exhibit elevated specific star formation rates (sSFRs) compared with typical MS galaxies. For the components with ALMA detection, from the total SFR_{IR+UV} and stellar masses, we obtain sSFR = 2.5–100 Gyr^{-1}. Considering the MS as defined in Schreiber et al. (2015), the distance to the MS is in the range $sSFR/sSFR_{MS} = 0.5$–22, calculated at the redshift of each source. Consequently, all of the sources studied here would formally fall into the starburst regime, with AK03 on the MS but also consistent with the starburst region, given its large SFR uncertainty (see Figure 5). If an important fraction of the stellar mass is undetectable hidden beneath the dust, the objects will move toward smaller distances to the MS, as represented by the bottom arrows in Figure 5.

6. Stellar Mass–Size Plane: Evolution to cQGs

The similar stellar mass and rest-frame optical/UV size distribution of $z > 3$ SMGs and cQGs at $z \sim 2$ have been used to argue for a direct evolutionary connection between the two populations (Toft et al. 2014). However, the stellar mass builds up in the nuclear starburst. At the derived SFR and stellar mass for our sample, approximately half of the descendant stellar mass would be formed during the starburst phase. The FIR size traces the region where the starburst is taking place; thus, it is the relevant measurement to compare to the optical size in the descendant 1–2 Gyr later, as it is the best proxy for the location of the bulk of the stellar mass once the starburst is finished.

In Figure 6, we compare the stellar masses and rest-frame FIR effective radii for our sample of SMGs to the stellar masses and rest-frame optical effective radii measured for spectroscopically confirmed cQGs at $1.8 < z < 2.5$ (samples from van de Sande et al. 2013; Krogager et al. 2014; Belli et al. 2017). Note that the optical sizes in these cQG comparison samples were also obtained by fitting the two-dimensional surface brightness distribution with GALFIT, as we did for the FIR sizes of our SMG sample.

The SMGs appear offset to smaller stellar masses and sizes than the cQGs, with approximately the same scatter. The median stellar mass of our SMGs is $\log(M_*/M_\odot) = 10.49 \pm 0.32$, compared to $\log(M_*/M_\odot) = 11.07 \pm 0.08$ for the cQGs. The median rest-frame FIR size for the SMGs is $r_e = 0.70 \pm 0.29$ kpc, compared to a rest-frame optical size of $r_e = 1.61 \pm 0.68$ kpc for the cQGs. The SMGs would have to increase in both stellar mass and size to evolve into $z \sim 2$ cQGs.

In the following, we discuss whether such an evolution is plausible, given the observed properties of the SMG sample.

As the galaxies are undergoing starbursts, they will grow significantly in stellar mass before quenching. Toft et al. (2014) derived a depletion timescale of $\tau_{gas} = 42^{+0.40}_{-0.29}$ Myr for the number density of $z \gtrsim 3$ SMGs and cQGs at $z \sim 2$ to match. Assuming this number, at their current median $SFR_{IR+UV} = 920\ M_\odot\ yr^{-1}$, the stellar mass is expected to increase by a factor of ~2.24 (~0.35 dex). Star formation is not expected to increase the sizes significantly. The sizes of the remnants are, however, foreseen to grow due to ongoing minor mergers.

The median stellar mass ratio of the ongoing minor mergers is 6.5, and the average number of them is 1.2. Taking these mergers into account, the expected increase in stellar mass is ~2.43 (~0.39 dex). Adopting the simple models of Bezanson et al. (2009) for size growth due to minor mergers, the remnants are expected to grow by a factor of ~1.39 (~0.14 dex).

Simulations suggest a typical minor merger timescale of 0.49 ± 0.24 Gyr (Lotz et al. 2010). This provides sufficient time for the mergers to complete in the range $z \sim 4.5$–3.5 while

not violating the stellar ages of 1–2 Gyr derived for $z \sim 2.5$–2.0 cQGs (Toft et al. 2012).

The combined average stellar mass and size growth anticipated from completion of the starburst and the minor mergers is shown as the solid arrow in the bottom right of Figure 6. The SMGs would grow to a stellar mass of $\log(M_*/M_\odot) = 10.88 \pm 0.32$ and a size of $r_e = 0.98 \pm 0.29$ kpc, bringing the two populations into agreement within the uncertainties.

The scenario laid out here is in line with recent theoretical work by Faisst et al. (2017b), which suggests that models with starburst-induced compaction followed by minor merger growth better reproduce the sizes of the quenched remnants than models without structural changes.

In order to provide the stellar mass increase, the SMGs need enough gas reservoir to fuel the star formation. The median gas mass for our sample calculated from $M_{\rm dust}$ using a GDR = 90 is $3.7 \times 10^{11}\ M_\odot$. The factor of ∼2.24 mentioned above means the creation of $3.8 \times 10^{10}\ M_\odot$, which would be achieved with an ∼10% efficiency of converting gas into stars. The available molecular gas estimates derived from ^{12}CO measurements in the literature for our sample are: AzTEC1, $M_{\rm H2} = 1.4 \pm 0.2 \times 10^{11}\ M_\odot$, with $\tau_{\rm gas} \sim 200$ Myr (Yun et al. 2015); AzTEC/C159, $M_{\rm H2} = 1.5 \pm 0.3 \times 10^{11}\ M_\odot$, with $\tau_{\rm gas} = 200 \pm 100$ Myr (Jiménez-Andrade et al. 2018); and J1000+0234, $M_{\rm H2} = 2.6 \times 10^{10}\ M_\odot$, with $\tau_{\rm gas} \sim 30$ Myr (Schinnerer et al. 2008). The amount of gas available to form stars seems enough to account for the expected increase in stellar mass, and the short depletion timescale matches the short duration of the SMG phase of ∼100 Myr (e.g., Tacconi et al. 2006, 2008).

In the proposed scenario, we assume that the rest-frame FIR dust continuum is a reasonable proxy for the effective star-forming region. The [C II] size estimates for a subset of our sample (A. Karim et al. 2018, in preparation) are typically two times larger, which is in agreement with other studies finding larger [C II] sizes compared with dust continuum sizes (e.g., Riechers et al. 2014a; Díaz-Santos et al. 2016; Oteo et al. 2016). Considering a scenario with $\tau_{\rm gas} = 100$ Myr and [C II] sizes would mean a factor of ∼3.96 (∼0.60 dex) change in stellar mass and ∼2.78 (∼0.44 dex) in size, still suitable for the two populations to match, with the SMGs having a final stellar mass of $\log(M_*/M_\odot) = 11.09 \pm 0.32$ and size of $r_e = 1.95 \pm 0.29$ kpc.

7. Discussion

In this work, we present detailed observations of a small sample of $z \sim 4.5$–3.5 SMGs and argue that their properties are consistent with being progenitors of ∼2.5–2.0 cQGs.

We demonstrated that the distribution of the two populations in the stellar mass–size plane is consistent when accounting for stellar mass and size growth expected from the completion of the ongoing starbursts and subsequent merging with minor companions.

These conclusions are based on small samples for both the SMGs and cQGs, possibly subject to selection biases, and apply only in two broad redshift intervals. To further explore the evolutionary connection between the two populations, larger uniform samples with a finer redshift sampling are needed. For example, cQGs are now being identified out to $z \sim 4$ (Straatman et al. 2015), although confirming quiescent galaxies at this high redshift can be challenging (Glazebrook et al. 2017; Schreiber et al. 2017; Simpson et al. 2017). If the proposed connection holds at all redshifts, the properties of these should match those of SMGs at $z > 6$ (e.g., Riechers et al. 2013; Decarli et al. 2017; Riechers et al. 2017; Strandet et al. 2017). Similarly, the properties of $z \sim 2$ SMGs should match those of 1 Gyr old quiescent galaxies at $z \sim 1.5$.

A crucial measure placing starburst galaxies in a cosmic evolution context is their stellar mass. Unfortunately, it is very difficult to derive due to large amounts of dust that may prevent an unknown fraction of the stellar light from escaping, even at rest-frame near-IR wavelengths. Perhaps the best way forward is to measure it indirectly as the difference between the total dynamical mass and the gas mass (and dark matter), both of which can be estimated from molecular-line observations with ALMA (A. Karim et al. 2018, in preparation).

What triggers high-redshift starbursts remains unclear. All of the galaxies studied here showed evidence of ongoing minor mergers, and this could be the process responsible for igniting the starburst, while only one showed evidence of an ongoing major merger. Bustamante et al. (2017) recently stated that while strong starbursts are likely to occur in a major merger, they can also originate from minor mergers if more than two galaxies interact. This suggests that the triggering processes at high redshift are different from those at low redshift, where the most luminous starburst galaxies are almost exclusively associated with major mergers, which would also be in agreement with recent theoretical work (Narayanan et al. 2015). Nevertheless, low-redshift, lower-luminosity LIRGs are also found to be associated with minor mergers. The difference could actually be due to the gas fraction of the most massive component in the interaction, which is higher at high redshift than at low redshift; thus, it may allow for a relatively more intense starburst to occur in the presence of a minor merger at high redshift than at low redshift.

However, even at the relatively high spatial resolution obtained in this study, we are not able to rule out close ongoing major mergers. As an example, the nucleus of the archetypical starburst galaxy Arp 220 breaks into two components separated by ∼350 pc (Scoville et al. 2017). At $z = 4.5$, this corresponds to an angular separation of ∼0.″05; thus, we would not be able to resolve this particular case at our current resolution (median synthesized beam size 0.″30 × 0.″27). However, the nearby FIR peaks in two of our systems that we are able to resolve, and the color gradients over all the galaxies would be consistent with such a picture.

An alternative plausible scenario would be that the starburst episode we are witnessing would indeed be triggered by previous minor or major mergers that we are currently unable to detect. The minor companions we detect here would be mergers in an early phase prior to coalescence but not responsible for the observed starburst episode. Gas dynamics in these systems show evidence for rotationally supported star-forming disks (Jones et al. 2017; Jiménez-Andrade et al. 2018, A. Karim et al. 2018, in preparation), which would have to be triggered by either gravitational instabilities or highly dissipational mergers that quickly set into a disk configuration. Smooth accretion can also trigger high SFR while still maintaining a rotationally supported disk (e.g., Romano-Díaz et al. 2014). Some simulations of galaxy formation at high redshift have also shown that gas and stellar disks already exist at $z \gtrsim 6$ (e.g., Pawlik et al. 2011; Romano-Díaz et al. 2011; Feng et al. 2015; Pallottini et al. 2017).

Recently, a population of compact star-forming galaxies (cSFGs) at $2.0 < z < 3.0$ have been suggested as progenitors for cQGs (e.g., Barro et al. 2013; van Dokkum et al. 2015; Barro et al. 2016). Two different progenitor populations are not necessarily mutually exclusive. Both SMGs and cSFGs could be part of the same global population but observed in a different phase or intensity of the stellar mass assembly, with the SMGs reflecting the peak of the process and the cSFGs being a later stage. The cSFGs are consistent with an intermediate population between $z > 3$ SMGs and $z \sim 2$ cQGs, caught in a phase where the star formation is winding down and a compact remnant is emerging, transitioning from the region above the MS of star-forming galaxies (Barro et al. 2017) to the MS (Popping et al. 2017a) and eventually below it. In fact, Elbaz et al. (2017) recently showed that starburst galaxies exist both above and within the MS. The increased AGN fraction in cSFGs suggests that they are entering an AGN/QSO quenching phase, which could be responsible for shutting down the residual star formation, leaving behind compact stellar remnants to develop into $z \sim 2$ cQGs (Barro et al. 2013; see also Sanders et al. 1988; Hopkins et al. 2006; Hickox et al. 2012; Wilkinson et al. 2017).

In order to further explore the evolutionary connection between SMGs, cSFGs, and cQGs, larger spectroscopic samples are needed. High spatial resolution rest-frame optical/FIR observations are paramount to unveiling their different subcomponents, measuring accurate optical/FIR sizes and stellar masses, and uncovering the underlying structure of the dust. In this context, *JWST* observations of DSFGs at high redshift will revolutionize our understanding of galaxy mass assembly through cosmic time.

8. Summary and Conclusions

A sample of six SMGs, five of which are spectroscopically confirmed to be at $z \sim 4.5$, were imaged at high spatial resolution with *HST*, probing rest-frame UV stellar emission, and with ALMA, probing the rest-frame FIR dust continuum emission. We find the following.

1. The rest-frame UV emission appears irregular and more extended than the very compact rest-frame FIR emission, which exhibits a median physical size of $r_e = 0.70 \pm 0.29$ kpc.
2. The *HST* images reveal that the systems are composed of multiple merging components. The dust emission pinpointing the bulk of star formation is associated with the reddest and most massive component of the merger. The companions are bluer, lower-mass galaxies with properties typical of normal star-forming galaxies at similar redshifts.
3. We find morphological evidence suggesting that the lack of spatial coincidence between the rest-frame UV and FIR emissions is the primary cause for the elevated position of DSFGs in the IRX–β plane. This has consequences for energy balance modeling efforts, which must account for the implied high extinction.
4. A stellar mass analysis reveals that only one of the systems is undergoing a major merger. On the other hand, all of the systems are undergoing at least one minor merger with a median stellar mass ratio of 1:6.5. In addition, the *HST* images hint at the presence of additional nearby low-mass systems.
5. The stellar masses and rest-frame FIR sizes of the $z \sim 4.5$ SMGs fall on the stellar mass–rest-frame optical size relation of $z \sim 2$ cQGs, but spanning lower stellar masses and smaller sizes. To evolve into $z \sim 2$ cQGs, the SMGs must increase in both stellar mass and size. We show that the expected growth due to the ongoing starburst and minor mergers can account for such evolution.

   Minor merging thus appears to play a pivotal role in the evolution of massive elliptical galaxies throughout their full cosmic history, both for their size evolution from $z = 2$ to $z = 0$ (e.g., Naab et al. 2009; Newman et al. 2012) and for their formation at higher redshifts.

We thank I. Smail for his detailed comments and suggestions that help improve this manuscript; J. M. Simpson for providing the SCUBA2 data; C. Y. Peng and G. Barro for their advice on `GALFIT`; S. Zibetti for his support with `ADAPTSMOOTH`; C. M. Casey for providing the DSFG comparison data plotted in Figure 4; and D. Watson, J. Hjorth, I. Davidzon, H. Rhodin, K. K. Knudsen, P. Laursen, D. B. Sanders, M. P. Haynes, R. Pavesi, T. K. D. Leung, and S. Martín-Álvarez for helpful comments and suggestions. We are grateful to the anonymous referee, whose comments have been very useful to improving our work.

C.G.G. and S.T. acknowledge support from the European Research Council (ERC) Consolidator Grant funding scheme (project ConTExt, grant number 648179). A.K., E.J.A., and F.B. acknowledge support by the Collaborative Research Centre 956, subproject A1, funded by the Deutsche Forschungsgemeinschaft (DFG). Support for B.M. was provided by the DFG priority program 1573, "The physics of the interstellar medium." D.R. acknowledges support from the National Science Foundation under grant number AST-1614213. V.S. acknowledges support from the European Union's Seventh Framework program under grant agreement 337595 (ERC Starting Grant, "CoSMass"). M.A. acknowledges partial support from FONDECYT through grant 1140099. ERD also acknowledge support by the Collaborative Research Centre 956, subproject C4, funded by the DFG. M.J.M. acknowledges the support of the National Science Centre, Poland, through POLONEZ grant 2015/19/P/ST9/04010; this project has received funding from the European Union's Horizon 2020 research and innovation program under Marie Skłodowska-Curie grant agreement No. 665778.

Based on observations made with the NASA/ESA *Hubble Space Telescope*, obtained at the Space Telescope Science Institute, which is operated by the Association of Universities for Research in Astronomy, Inc., under NASA contract NAS 5-26555. These observations are associated with program #13294. Support for program #13294 was provided by NASA through a grant from the Space Telescope Science Institute.

This research made use of the following ALMA data: ADS/JAO.ALMA#2012.1.00978.S. ALMA is a partnership of the ESO (representing its member states), NSF (USA), and NINS (Japan), together with the NRC (Canada) and NSC and ASIAA (Taiwan), in cooperation with the Republic of Chile. The Joint ALMA Observatory is operated by the ESO, AUI/NRAO, and NAOJ.

This paper employed `Astropy`, a community-developed core Python package for Astronomy (Astropy Collaboration et al. 2013); `APLpy`, an open-source plotting package for Python (Robitaille & Bressert 2012); CASA (McMullin

et al. 2007); Matplotlib (Hunter 2007); Numpy; Photutils (Bradley et al. 2016); PyBDSF; and R, a language and environment for statistical computing.

ORCID iDs

C. Gómez-Guijarro https://orcid.org/0000-0002-4085-9165
S. Toft https://orcid.org/0000-0003-3631-7176
A. Karim https://orcid.org/0000-0002-8414-9579
B. Magnelli https://orcid.org/0000-0002-6777-6490
G. E. Magdis https://orcid.org/0000-0002-4872-2294
E. F. Jiménez-Andrade https://orcid.org/0000-0002-2640-5917
F. Fraternali https://orcid.org/0000-0002-0447-3230
S. Fujimoto https://orcid.org/0000-0001-7201-5066
D. A. Riechers https://orcid.org/0000-0001-9585-1462
E. Schinnerer https://orcid.org/0000-0002-3933-7677
V. Smolčić https://orcid.org/0000-0002-3893-8614
M. Aravena https://orcid.org/0000-0002-6290-3198
F. Bertoldi https://orcid.org/0000-0002-1707-1775
G. Hasinger https://orcid.org/0000-0002-0797-0646
G. C. Jones https://orcid.org/0000-0002-0267-9024
A. M. Koekemoer https://orcid.org/0000-0002-6610-2048
N. Lee https://orcid.org/0000-0001-7348-2926
H. J. McCracken https://orcid.org/0000-0002-9489-7765
M. J. Michałowski https://orcid.org/0000-0001-9033-4140
F. Navarrete https://orcid.org/0000-0002-3647-5599
A. Puglisi https://orcid.org/0000-0001-9369-1805
E. Romano-Díaz https://orcid.org/0000-0002-0071-3217
K. Sheth https://orcid.org/0000-0002-5496-4118
J. D. Silverman https://orcid.org/0000-0002-0000-6977
J. Staguhn https://orcid.org/0000-0002-8437-0433
C. L. Steinhardt https://orcid.org/0000-0003-3780-6801
M. Tanaka https://orcid.org/0000-0002-5011-5178
F. Valentino https://orcid.org/0000-0001-6477-4011
E. van Kampen https://orcid.org/0000-0002-6327-5154
A. Zirm https://orcid.org/0000-0002-6707-275X

References

Andrews, B. H., & Thompson, T. A. 2011, ApJ, 727, 97
Arnouts, S., Cristiani, S., Moscardini, L., et al. 1999, MNRAS, 310, 540
Astropy Collaboration, Robitaille, T. P., Tollerud, E. J., et al. 2013, A&A, 558, A33
Barisic, I., Faisst, A. L., Capak, P. L., et al. 2017, ApJ, 845, 41
Barro, G., Faber, S. M., Pérez-González, P. G., et al. 2013, ApJ, 765, 104
Barro, G., Kriek, M., Pérez-González, P. G., et al. 2016, ApJL, 827, L32
Barro, G., Kriek, M., Pérez-González, P. G., et al. 2017, ApJL, 851, L40
Belli, S., Newman, A. B., & Ellis, R. S. 2017, ApJ, 834, 18
Berta, S., Lutz, D., Genzel, R., Förster-Schreiber, N. M., & Tacconi, L. J. 2016, A&A, 587, A73
Bertin, E. 2010, SWarp: Resampling and Co-adding FITS Images Together, Astrophysics Source Code Library, ascl:1010.068
Bertin, E., & Arnouts, S. 1996, A&AS, 117, 393
Bezanson, R., van Dokkum, P. G., Tal, T., et al. 2009, ApJ, 697, 1290
Blain, A. W., Chapman, S. C., Smail, I., & Ivison, R. 2004, ApJ, 611, 725
Blain, A. W., Smail, I., Ivison, R. J., Kneib, J.-P., & Frayer, D. T. 2002, PhR, 369, 111
Bouwens, R. J., Illingworth, G. D., Franx, M., et al. 2009, ApJ, 705, 936
Bradley, L., Sipocz, B., Robitaille, T., et al. 2016, Photutils: Photometry tools, Astrophysics Source Code Library, ascl:1609.011
Brammer, G. B., van Dokkum, P. G., Franx, M., et al. 2012, ApJS, 200, 13
Brammer, G. B., Whitaker, K. E., van Dokkum, P. G., et al. 2011, ApJ, 739, 24
Brisbin, D., Miettinen, O., Aravena, M., et al. 2017, A&A, 608, A15
Bruzual, G., & Charlot, S. 2003, MNRAS, 344, 1000
Buat, V., Iglesias-Páramo, J., Seibert, M., et al. 2005, ApJL, 619, L51
Bustamante, S., Sparre, M., Springel, V., & Grand, R. J. J. 2017, MNRAS, submitted (arXiv:1712.03250)
Calura, F., Pozzi, F., Cresci, G., et al. 2017, MNRAS, 465, 54
Calzetti, D., Armus, L., Bohlin, R. C., et al. 2000, ApJ, 533, 682
Capak, P., Aussel, H., Ajiki, M., et al. 2007, ApJS, 172, 99
Capak, P., Carilli, C. L., Lee, N., et al. 2008, ApJL, 681, L53
Capak, P. L., Carilli, C., Jones, G., et al. 2015, Natur, 522, 455
Capak, P. L., Riechers, D., Scoville, N. Z., et al. 2011, Natur, 470, 233
Casey, C. M., Chen, C.-C., Cowie, L. L., et al. 2013, MNRAS, 436, 1919
Casey, C. M., Narayanan, D., & Cooray, A. 2014a, PhR, 541, 45
Casey, C. M., Scoville, N. Z., Sanders, D. B., et al. 2014b, ApJ, 796, 95
Castellano, M., Fontana, A., Grazian, A., et al. 2012, A&A, 540, A39
Chabrier, G. 2003, PASP, 115, 763
Chapman, S. C., Blain, A. W., Smail, I., & Ivison, R. J. 2005, ApJ, 622, 772
Chen, C.-C., Hodge, J. A., Smail, I., et al. 2017, ApJ, 846, 108
Chen, C.-C., Smail, I., Swinbank, A. M., et al. 2015, ApJ, 799, 194
Cimatti, A., Cassata, P., Pozzetti, L., et al. 2008, A&A, 482, 21
Civano, F., Marchesi, S., Comastri, A., et al. 2016, ApJ, 819, 62
Conselice, C. J., Bershady, M. A., Dickinson, M., & Papovich, C. 2003, AJ, 126, 1183
da Cunha, E., Charlot, S., & Elbaz, D. 2008, MNRAS, 388, 1595
Daddi, E., Dannerbauer, H., Stern, D., et al. 2009, ApJ, 694, 1517
Daddi, E., Dickinson, M., Morrison, G., et al. 2007, ApJ, 670, 156
Davidzon, I., Ilbert, O., Laigle, C., et al. 2017, A&A, 605, A70
Decarli, R., Walter, F., Venemans, B. P., et al. 2017, Natur, 545, 457
Díaz-Santos, T., Assef, R. J., Blain, A. W., et al. 2016, ApJL, 816, L6
Draine, B. T., & Li, A. 2007, ApJ, 657, 810
Elbaz, D., Daddi, E., Le Borgne, D., et al. 2007, A&A, 468, 33
Elbaz, D., Leiton, R., Nagar, N., et al. 2017, arXiv:1711.10047
Faisst, A. L., Capak, P. L., Yan, L., et al. 2017a, ApJ, 847, 21
Faisst, A. L., Carollo, C. M., Capak, P. L., et al. 2017b, ApJ, 839, 71
Feng, Y., Di Matteo, T., Croft, R., et al. 2015, ApJL, 808, L17
Finkelstein, S. L., Papovich, C., Salmon, B., et al. 2012, ApJ, 756, 164
Fudamoto, Y., Oesch, P. A., Schinnerer, E., et al. 2017, MNRAS, 472, 483
Fujimoto, S., Ouchi, M., Shibuya, T., & Nagai, H. 2017, ApJ, 850, 83
Glazebrook, K., Schreiber, C., Labbé, I., et al. 2017, Natur, 544, 71
Gonzaga, S., et al. 2012, The DrizzlePac Handbook (Baltimore, MD: STScI)
Grogin, N. A., Kocevski, D. D., Faber, S. M., et al. 2011, ApJS, 197, 35
Hainline, L. J., Blain, A. W., Smail, I., et al. 2011, ApJ, 740, 96
Hickox, R. C., Wardlow, J. L., Smail, I., et al. 2012, MNRAS, 421, 284
Hodge, J. A., Swinbank, A. M., Simpson, J. M., et al. 2016, ApJ, 833, 103
Hopkins, P. F., Somerville, R. S., Hernquist, L., et al. 2006, ApJ, 652, 864
Howell, J. H., Armus, L., Mazzarella, J. M., et al. 2010, ApJ, 715, 572
Hunter, J. D. 2007, CSE, 9, 90
Ikarashi, S., Ivison, R. J., Caputi, K. I., et al. 2015, ApJ, 810, 133
Ilbert, O., Arnouts, S., McCracken, H. J., et al. 2006, A&A, 457, 841
Jiménez-Andrade, E. F., Magnelli, B., Karim, A., et al. 2018, A&A, in press (arXiv:1710.10181)
Jones, G. C., Carilli, C. L., Shao, Y., et al. 2017, ApJ, 850, 180
Kaviraj, S., Peirani, S., Khochfar, S., Silk, J., & Kay, S. 2009, MNRAS, 394, 1713
Kennicutt, R. C., Jr. 1998, ARA&A, 36, 189
Koekemoer, A. M., Aussel, H., Calzetti, D., et al. 2007, ApJS, 172, 196
Koekemoer, A. M., Faber, S. M., Ferguson, H. C., et al. 2011, ApJS, 197, 36
Kriek, M., Conroy, C., van Dokkum, P. G., et al. 2016, Natur, 540, 248
Krogager, J.-K., Zirm, A. W., Toft, S., Man, A., & Brammer, G. 2014, ApJ, 797, 17
Laigle, C., McCracken, H. J., Ilbert, O., et al. 2016, ApJS, 224, 24
Lotz, J. M., Jonsson, P., Cox, T. J., et al. 2011, ApJ, 742, 103
Lotz, J. M., Jonsson, P., Cox, T. J., & Primack, J. R. 2010, MNRAS, 404, 575
Lutz, D., Berta, S., Contursi, A., et al. 2016, A&A, 591, A136
Magdis, G. E., Daddi, E., Béthermin, M., et al. 2012, ApJ, 760, 6
Magdis, G. E., Rigopoulou, D., Daddi, E., et al. 2017, A&A, 603, A93
Magdis, G. E., Rigopoulou, D., Huang, J.-S., & Fazio, G. G. 2010, MNRAS, 401, 1521
Man, A. W. S., Zirm, A. W., & Toft, S. 2016, ApJ, 830, 89
Marchesi, S., Civano, F., Elvis, M., et al. 2016, ApJ, 817, 34
Marques-Chaves, R., Pérez-Fournon, I., Gavazzi, R., et al. 2018, ApJ, 854, 151
Martí-Vidal, I., Vlemmings, W. H. T., Muller, S., & Casey, S. 2014, A&A, 563, A136
McCracken, H. J., Milvang-Jensen, B., Dunlop, J., et al. 2012, A&A, 544, A156
McMullin, J. P., Waters, B., Schiebel, D., Young, W., & Golap, K. 2007, in ASP Conf. Ser. 376, Astronomical Data Analysis Software and Systems XVI, ed. R. A. Shaw, F. Hill, & D. J. Bell (San Francisco, CA: ASP), 127
Meurer, G. R., Heckman, T. M., & Calzetti, D. 1999, ApJ, 521, 64
Michałowski, M., Hjorth, J., & Watson, D. 2010, A&A, 514, A67
Michałowski, M. J., Dunlop, J. S., Cirasuolo, M., et al. 2012, A&A, 541, A85

Michałowski, M. J., Dunlop, J. S., Koprowski, M. P., et al. 2017, MNRAS, 469, 492
Michałowski, M. J., Hayward, C. C., Dunlop, J. S., et al. 2014, A&A, 571, A75
Miettinen, O., Delvecchio, I., Smolčić, V., et al. 2017, A&A, 606, A17
Miettinen, O., Smolčić, V., Novak, M., et al. 2015, A&A, 577, A29
Momcheva, I. G., Brammer, G. B., van Dokkum, P. G., et al. 2016, ApJS, 225, 27
Monet, D. G., Levine, S. E., Canzian, B., et al. 2003, AJ, 125, 984
Naab, T., Johansson, P. H., & Ostriker, J. P. 2009, ApJL, 699, L178
Narayanan, D., Davé, R., Johnson, B. D., et al. 2018, MNRAS, 474, 1718
Narayanan, D., Turk, M., Feldmann, R., et al. 2015, Natur, 525, 496
Newman, A. B., Ellis, R. S., Bundy, K., & Treu, T. 2012, ApJ, 746, 162
Noeske, K. G., Weiner, B. J., Faber, S. M., et al. 2007, ApJL, 660, L43
Oke, J. B. 1974, ApJS, 27, 21
Oser, L., Naab, T., Ostriker, J. P., & Johansson, P. H. 2012, ApJ, 744, 63
Oteo, I., Ivison, R. J., Dunne, L., et al. 2016, ApJ, 827, 34
Oteo, I., Ivison, R. J., Negrello, M., et al. 2017, arXiv:1709.04191
Overzier, R. A., Heckman, T. M., Wang, J., et al. 2011, ApJL, 726, L7
Pallottini, A., Ferrara, A., Gallerani, S., et al. 2017, MNRAS, 465, 2540
Pawlik, A. H., Milosavljević, M., & Bromm, V. 2011, ApJ, 731, 54
Peng, C. Y., Ho, L. C., Impey, C. D., & Rix, H.-W. 2002, AJ, 124, 266
Pope, A., Chary, R.-R., Alexander, D. M., et al. 2008, ApJ, 675, 1171
Popping, G., Decarli, R., Man, A. W. S., et al. 2017a, A&A, 602, A11
Popping, G., Puglisi, A., & Norman, C. A. 2017b, MNRAS, 472, 2315
Popping, G., Somerville, R. S., & Galametz, M. 2017c, MNRAS, 471, 3152
Puglisi, A., Daddi, E., Renzini, A., et al. 2017, ApJL, 838, L18
Ricciardelli, E., Trujillo, L., Buitrago, F., & Conselice, C. J. 2010, MNRAS, 406, 230
Riechers, D. A., Bradford, C. M., Clements, D. L., et al. 2013, Natur, 496, 329
Riechers, D. A., Capak, P. L., Carilli, C. L., et al. 2010, ApJL, 720, L131
Riechers, D. A., Carilli, C. L., Capak, P. L., et al. 2014a, ApJ, 796, 84
Riechers, D. A., Leung, T. K. D., Ivison, R. J., et al. 2017, ApJ, 850, 1
Riechers, D. A., Pope, A., Daddi, E., et al. 2014b, ApJ, 786, 31
Robitaille, T., & Bressert, E. 2012, APLpy: Astronomical Plotting Library in Python, Astrophysics Source Code Library, ascl:1208.017
Romano-Díaz, E., Choi, J.-H., Shlosman, I., & Trenti, M. 2011, ApJL, 738, L19
Romano-Díaz, E., Shlosman, I., Choi, J.-H., & Sadoun, R. 2014, ApJL, 790, L32
Safarzadeh, M., Hayward, C. C., & Ferguson, H. C. 2017, ApJ, 840, 15
Salim, S., Rich, R. M., Charlot, S., et al. 2007, ApJS, 173, 267
Sanders, D. B., & Mirabel, I. F. 1996, ARA&A, 34, 749
Sanders, D. B., Salvato, M., Aussel, H., et al. 2007, ApJS, 172, 86
Sanders, D. B., Soifer, B. T., Elias, J. H., et al. 1988, ApJ, 325, 74
Schinnerer, E., Carilli, C. L., Capak, P., et al. 2008, ApJL, 689, L5
Schinnerer, E., Carilli, C. L., Scoville, N. Z., et al. 2004, AJ, 128, 1974
Schreiber, C., Labbé, I., Glazebrook, K., et al. 2017, arXiv:1709.03505
Schreiber, C., Pannella, M., Elbaz, D., et al. 2015, A&A, 575, A74
Scoville, N., Aussel, H., Brusa, M., et al. 2007, ApJS, 172, 1
Scoville, N., Murchikova, L., Walter, F., et al. 2017, ApJ, 836, 66
Shen, S., Mo, H. J., White, S. D. M., et al. 2003, MNRAS, 343, 978
Simpson, J. M., Smail, I., Swinbank, A. M., et al. 2015, ApJ, 799, 81
Simpson, J. M., Smail, I., Wang, W.-H., et al. 2017, ApJL, 844, L10
Simpson, J. M., Swinbank, A. M., Smail, I., et al. 2014, ApJ, 788, 125
Skelton, R. E., Whitaker, K. E., Momcheva, I. G., et al. 2014, ApJS, 214, 24
Smolčić, V., Aravena, M., Navarrete, F., et al. 2012, A&A, 548, A4
Smolčić, V., Capak, P., Ilbert, O., et al. 2011, ApJL, 731, L27
Smolčić, V., Karim, A., Miettinen, O., et al. 2015, A&A, 576, A127
Smolčić, V., Miettinen, O., Tomičić, N., et al. 2017, A&A, 597, A4
Spilker, J. S., Marrone, D. P., Aravena, M., et al. 2016, ApJ, 826, 112
Straatman, C. M. S., Labbé, I., Spitler, L. R., et al. 2015, ApJL, 808, L29
Strandet, M. L., Weiss, A., De Breuck, C., et al. 2017, ApJL, 842, L15
Strandet, M. L., Weiss, A., Vieira, J. D., et al. 2016, ApJ, 822, 80
Swinbank, A. M., Simpson, J. M., Smail, I., et al. 2014, MNRAS, 438, 1267
Szomoru, D., Franx, M., & van Dokkum, P. G. 2012, ApJ, 749, 121
Tacconi, L. J., Genzel, R., Smail, I., et al. 2008, ApJ, 680, 246
Tacconi, L. J., Neri, R., Chapman, S. C., et al. 2006, ApJ, 640, 228
Takeuchi, T. T., Yuan, F.-T., Ikeyama, A., Murata, K. L., & Inoue, A. K. 2012, ApJ, 755, 144
Tanaka, M., Hasinger, G., Silverman, J. D., et al. 2017, arXiv:1706.00566
Thomas, D., Maraston, C., Bender, R., & Mendes de Oliveira, C. 2005, ApJ, 621, 673
Toft, S., Gallazzi, A., Zirm, A., et al. 2012, ApJ, 754, 3
Toft, S., Smolčić, V., Magnelli, B., et al. 2014, ApJ, 782, 68
Toft, S., van Dokkum, P., Franx, M., et al. 2007, ApJ, 671, 285
Toft, S., Zabl, J., Richard, J., et al. 2017, Natur, 546, 510
van de Sande, J., Kriek, M., Franx, M., et al. 2013, ApJ, 771, 85
van der Wel, A., Franx, M., van Dokkum, P. G., et al. 2014, ApJ, 788, 28
van Dokkum, P. G., Franx, M., Kriek, M., et al. 2008, ApJL, 677, L5
van Dokkum, P. G., Nelson, E. J., Franx, M., et al. 2015, ApJ, 813, 23
Wardlow, J. L., Smail, I., Coppin, K. E. K., et al. 2011, MNRAS, 415, 1479
Watson, D. 2011, A&A, 533, A16
Weiß, A., De Breuck, C., Marrone, D. P., et al. 2013, ApJ, 767, 88
Whitaker, K. E., Pope, A., Cybulski, R., et al. 2017, ApJ, 850, 208
Wilkinson, A., Almaini, O., Chen, C.-C., et al. 2017, MNRAS, 464, 1380
Younger, J. D., Fazio, G. G., Huang, J.-S., et al. 2007, ApJ, 671, 1531
Younger, J. D., Fazio, G. G., Wilner, D. J., et al. 2008, ApJ, 688, 59
Yun, M. S., Aretxaga, I., Gurwell, M. A., et al. 2015, MNRAS, 454, 3485
Zibetti, S. 2009, arXiv:0911.4956